

1 **Power spectral estimates using 2D Morlet-fan wavelets with emphasis on the long**
2 **wavelengths: jackknife errors, bandwidth resolution and orthogonality properties**

3

4 J. F. Kirby, and C. J. Swain

5 Department of Spatial Sciences, Curtin University, GPO Box U1987, Perth WA 6845,

6 Australia. E-mail: j.kirby@curtin.edu.au

7

8 Accepted *date*. Received *date*; in original form 2012 October 8

9

10 **Abbreviated title:** Long-wavelength power spectral estimation.

11

12 **Abstract**

13 We present a method for estimating the errors on local and global wavelet power spectra
14 using the jackknife approach to error estimation, and compare results with jackknifed
15 multitaper (MT) spectrum estimates. We test the methods on both synthetic and real data, the
16 latter being free air gravity over the Congo basin. To satisfy the independence requirement of
17 the jackknife we investigate the orthogonality properties of the two-dimensional Morlet
18 wavelet. Although Morlet wavelets are non-orthogonal, we show that careful selection of
19 parameters can yield approximate orthogonality in space and azimuth. We also find that,
20 when computed via the Fourier transform, the continuous wavelet transform (CWT) contains
21 errors at very long wavelengths due to the discretisation of large-scale wavelets in the Fourier
22 domain. We hence recommend the use of convolution in the space-domain at these scales,
23 even though this is computationally more expensive. Finally, in providing an investigation
24 into the bandwidth resolution of CWT and MT spectra and errors at long wavelengths, we
25 show that the Morlet wavelet is superior in this regard to Slepian tapers. Wavelets with higher

26 bandwidth-resolution deliver smaller spectral error estimates, in contrast to the MT method,
27 where tapers with higher bandwidth-resolution deliver larger errors. This results in the fan-
28 WT having better spectral estimation properties at long wavelengths than Slepian multitapers.

29

30 **Key words:** Fourier analysis; Numerical approximations and analysis; Wavelet transform;
31 Africa.

32

33 **1. Introduction**

34 Long-wavelength spectral estimates can be problematic. Banks *et al.* (2001) have drawn
35 attention to the “difficulty in correctly analysing features whose spatial scale is comparable
36 with the size of the data window”, and noted the significant differences between spectral
37 estimates of gravity, topography and their coherence made with different methods
38 (periodogram and multitaper) at wavelengths in the 1000 km range. More specifically,
39 Wieczorek & Simons (2005) show that (spherical) multitaper spectral estimates of data with a
40 red spectrum are significantly biased at wavenumbers smaller than the taper bandwidth. In
41 this study we provide a comparison between power spectra of two-dimensional (2D) signals
42 obtained from two methods: the fan wavelet transform using the Morlet wavelet (Kirby
43 2005), and the multitaper Fourier transform using Slepian tapers (Slepian 1978; Thomson
44 1982). We focus upon the long wavelengths of the spectra.

45

46 The wavelet transform was developed for the purpose of computing the ‘local spectrum’ of
47 non-stationary data (Grossman & Morlet 1984), that is, the power spectrum at a particular
48 location of data whose spectrum varies with time or space. One may also compute the ‘global
49 spectrum’ of the signal by averaging the local spectra over the spatial or temporal variable
50 (e.g., Torrence & Compo 1998). Such plots are commonly displayed in studies that also

51 compute the local spectrum (e.g., *Hudgins et al.* 1993; *Perrier et al.* 1995; *Kestin et al.* 1998;
52 *Torrence & Compo* 1998; *Shyu & Sun* 2002; *Bloomfield et al.* 2004; *Cazelles et al.* 2007),
53 and are useful in that they may be compared with the spectrum derived from the Fourier
54 transform, whether periodogram or multitaper. Since the Fourier spectrum and global wavelet
55 spectrum represent the power over the entire signal, they might be said to have limited
56 applicability to non-stationary data. Nevertheless they are both frequently used in spectral
57 analysis, unfortunately often without error estimates.

58

59 The provision of error estimates on power spectra is an important part of any scientific study
60 that uses them, but is one that is often neglected, especially in the wavelet literature. When
61 given, uncertainties are often presented as 95% confidence limits, computed under the
62 assumption of a χ^2 distribution for the power (*Torrence & Compo* 1998). To be meaningful,
63 this method requires the estimation (or assumption) of a background power spectrum and of
64 the number of degrees of freedom, both of which may be difficult to make reliably (*Percival*
65 *1995; Torrence & Compo* 1998).

66

67 Here we present an alternative method using the jackknife approach to error estimation
68 (*Thomson & Chave* 1991), and apply it to local and global wavelet power spectra. Our
69 analysis primarily concerns the 2D Morlet wavelet and 2D continuous wavelet transform
70 (CWT), but is readily adaptable to other wavelets, both continuous and discrete.

71

72 A requirement of the jackknife method is that the signal estimates to be jackknifed are
73 independent (*Thomson & Chave* 1991). While this would be satisfied by wavelet coefficients
74 that are obtained from orthogonal wavelets, the Morlet wavelet is non-orthogonal, giving
75 coefficients that are potentially correlated. Therefore we also provide a detailed investigation

76 of the conditions under which the 2D Morlet wavelet is approximately orthogonal, and use
77 only coefficients that have minimal leakage between them in order to apply the jackknife
78 method.

79

80 In the course of this study we also found that differences exist between wavelets defined in
81 the space-domain, and their counterparts defined in the Fourier domain. Since the use of the
82 Fourier method of CWT implementation is widespread (as opposed to space-domain
83 convolution), our findings reveal a potentially serious problem with this method.

84

85 We first introduce the CWT and some of its properties. We then discuss the 2D Morlet
86 wavelet and spectral estimation using the fan wavelet transform. This is followed by an
87 investigation into the behaviour of Morlet wavelets at large scales, their orthogonality
88 properties, and their bandwidth resolution. The application of the jackknife method of error
89 estimation to both local and global wavelet power spectra is then introduced. Finally the
90 methodology is applied to synthetic signals with a fractal spectrum, and to filtered signals in
91 an attempt to explore the wavenumber-domain resolution of the Morlet wavelet. We compare
92 our fan-WT spectra against those determined from the multitaper method.

93

94 **2. The Continuous Wavelet Transform**

95 **2.1 n -dimensional CWT**

96 The theory of the CWT is well known (Chui 1992; Kaiser 1994; Addison 2002; Antoine *et al.*
97 2004) but we present the basics here to familiarise readers with our notation. The CWT is a
98 convolution in the space (\mathbf{x}) domain between a signal, g , and the complex conjugate of a
99 daughter wavelet, $\psi_{s,\mathbf{t},\alpha}$, yielding wavelet coefficients, $\tilde{g}(s,\mathbf{t},\alpha)$. Note that the vector \mathbf{t} is not
100 time, but the spatial translation vector described below. For an n -dimensional signal:

101 $\tilde{g}(s, \mathbf{t}, \alpha) = \int_{R^n} g(\mathbf{x}) \psi_{s, \mathbf{t}, \alpha}^*(\mathbf{x}) d^n \mathbf{x} ,$ (1)

102 where the daughter wavelets are dilated, translated and rotated versions of a mother wavelet,

103 $\psi(\mathbf{x})$:

104 $\psi_{s, \mathbf{t}, \alpha}(\mathbf{x}) = s^{-n/2} \psi\left(\Omega(\alpha) \frac{\mathbf{x} - \mathbf{t}}{s}\right) .$ (2)

105 In eqs (1) and (2), s is the scale (dilation), \mathbf{t} is the translation vector, and Ω is the rotation
 106 matrix describing a rotation α (Farge 1992).

107

108 Convolution is computationally expensive, so the wavelet transform is commonly performed
 109 in the wavenumber (spatial frequency) domain as a multiplication of signal and wavelet
 110 Fourier transforms (\hat{g} and $\hat{\psi}_{s, \alpha}^*$, respectively) followed by inverse Fourier transformation.

111 For the n -dimensional wavenumber \mathbf{k} :

112 $\tilde{g}(s, \mathbf{t}, \alpha) = \mathbf{F}_n^{-1} \{ \hat{g}(\mathbf{k}) \hat{\psi}_{s, \alpha}^*(\mathbf{k}) \} ,$ (3)

113 where \mathbf{F}_n^{-1} is the n -dimensional inverse Fourier transform, and the mother-daughter
 114 relationship is:

115 $\hat{\psi}_{s, \alpha}(\mathbf{k}) = s^{n/2} \hat{\psi}(s \Omega(\alpha) \mathbf{k}) .$ (4)

116 In this study we focus on two-dimensional wavelets.

117

118 **2.2 Equivalent Fourier wavenumber**

119 Since wavelets are, in essence, bandpass filters, at each scale they can be assigned an
 120 ‘equivalent Fourier wavenumber’, representing the dominant harmonic of the signal that is
 121 preferentially passed. Here we use the peak wavenumber method, which gives the
 122 wavenumber at which the wavelet’s spectrum is a maximum (Addison 2002; Kirby 2005). In
 123 this case the equivalent Fourier wavenumber, κ , is calculated from the gradient of the wavelet

124 Fourier transform with respect to wavenumber. For 2D wavelets:

$$125 \quad \nabla_{\mathbf{k}} \hat{\psi}_{s,\alpha}(\mathbf{k}) \Big|_{\kappa} = 0 \quad , \quad (5)$$

126 where $\nabla_{\mathbf{k}} = (\partial / \partial k_x, \partial / \partial k_y)$. For most wavelets the equivalent Fourier wavenumber is

127 inversely proportional to scale.

128

129 **2.3 Scales**

130 In this study, as in others (Torrence & Compo 1998), we choose the wavelet scales in the

131 following manner. Take first the 1D case. For a discretised signal of N_x elements at a

132 sampling interval of Δx , we assume that the first harmonic in the signal that can be properly

133 represented has a wavelength equal to the length of the data series, $\lambda_{\max} = N_x \Delta x$ (Torrence &

134 Compo 1998), and a corresponding wavenumber of $k_{\min} = 2\pi / \lambda_{\max}$. The largest scale (s_1)

135 used in the CWT is then the scale at which the equivalent Fourier wavenumber for a given

136 wavelet has a value of k_{\min} .

137

138 The scales are then evaluated according to an octave decomposition (Torrence & Compo

139 1998). The j^{th} scale is:

$$140 \quad s_j = s_1 2^{-(j-1)/\nu} \quad , \quad j = [1, N_s] \quad , \quad (6)$$

141 where ν is the number of scales per octave (or ‘voices’), and N_s is the number of scales. In

142 order to calculate N_s we assume that the last harmonic in the signal that can be properly

143 resolved has a wavenumber no greater than the Nyquist wavenumber of the signal, $k_{\text{Nyq}} = 2\pi /$

144 $(2\Delta x)$. The number of scales is then obtained from (6):

$$145 \quad N_s = 1 + \nu \log_2 \left(\frac{k_{\text{Nyq}}}{k_{\min}} \right) \quad . \quad (7)$$

146 As in 1D, scales in 2D are defined by the data set size and sampling interval, though for non-

147 square areas and unequal sampling intervals we use the smallest numerical values of N_x and
148 N_y , and of Δx and Δy .

149

150 **2.4 Cone of influence**

151 We also define here the cone of influence (COI) for a wavelet (Torrence & Compo 1998).

152 Regions within the COI are suggested to have wavelet coefficients that are contaminated by
153 edge effects due to discontinuities at the data boundaries and may be omitted. Generally, the
154 width of the COI is defined as the distance from the peak of the space domain wavelet to the
155 point at which the envelope of the wavelet decays to a fraction q_{coi} of its peak amplitude (q_{coi}
156 < 1). Some studies take $q_{coi} = e^{-1}$ and call it the ‘ e -folding distance’ (Torrence & Compo
157 1998), but other definitions are possible, for example $q_{coi} = 0.5$ (see Section 4).

158

159 **3. Power Spectral Estimation**

160 **3.1 Fan wavelet spectra**

161 Unlike isotropic wavelets, 2D anisotropic wavelets can be arranged in angular superpositions,
162 in a ‘fan’ geometry by rotation (Antoine *et al.* 2004; Kirby 2005). If the particular geometry
163 is chosen correctly, then the superposition can yield wavelet coefficients that are both
164 isotropic and complex (Kirby 2005), in contrast to the use of real-valued wavelets whose
165 coefficients are isotropic but real-valued, or to the use of single anisotropic wavelets which
166 yield complex but anisotropic coefficients.

167

168 This ability of the fan wavelet transform, to yield complex, isotropic wavelet coefficients, has
169 driven its use in the estimation of the complex coherency between two surfaces (Kirby &
170 Swain 2004, 2009), and in the identification of incoherent noise (Kirby & Swain 2009). The
171 major application has been mainly in studies of the effective elastic thickness of the

172 lithosphere and its anisotropic variations (e.g., Kirby & Swain 2004, 2006; Audet &
 173 Mareschal 2007), but also in fringe pattern analysis in optics (e.g., Gdeisat *et al.* 2006; Li *et*
 174 *al.* 2009). There is also scope for applications to potential field transformations such as
 175 upward continuation, where the continuation level varies with location, and to estimating
 176 spectra of aeromagnetic maps for Curie depth estimation.

177

178 Power spectra obtained from fan superpositions are obtained by first computing a series of
 179 anisotropic wavelet coefficients at different azimuths, $\tilde{g}(s, \mathbf{t}, \alpha)$. The power spectrum at each
 180 azimuth and location is:

$$181 \quad P(s, \mathbf{x}, \alpha) = |\tilde{g}(s, \mathbf{x}, \alpha)|^2, \quad (8)$$

182 now writing \mathbf{x} for \mathbf{t} . The local fan wavelet power spectrum (or ‘scalogram’) is a superposition
 183 of eq. (8) over azimuth:

$$184 \quad P(s, \mathbf{x}) = \frac{1}{N_\alpha} \sum_{j=1}^{N_\alpha} P(s, \mathbf{x}, \alpha_j). \quad (9)$$

185 In eq. (9) $\alpha_j = (j-1)\delta\alpha$, where $\delta\alpha$ is the angular separation between wavelets: its particular
 186 value for the Morlet wavelet will be derived in Section 6. The number of wavelets in a fan is
 187 N_α . If the azimuths cover π radians then isotropy (independence of azimuth) is achieved
 188 (Kirby 2005), and:

$$189 \quad N_\alpha = \left\lfloor \frac{\pi}{\delta\alpha} \right\rfloor, \quad (10)$$

190 where, for some real number a , $\lfloor a \rfloor$ indicates the greatest integer $\leq a$.

191

192 The ‘global’ power spectrum is derived by averaging the local scalogram values over space,
 193 at each scale:

194
$$P(s) = \frac{1}{N_{xy}} \sum_{n=1}^{N_{xy}} P(s, \mathbf{x}_n) \quad (11)$$

195 (Torrence & Compo 1998), where $P(s, \mathbf{x})$ is given by eq. (9), and $N_{xy} = N_x N_y$, the total number
 196 of space domain grid nodes.

197

198 **3.2 Multitaper spectra**

199 The multitaper (MT) method is a commonly-used technique to estimate power spectra
 200 (Thomson 1982), in both one and two dimensions. Our MT spectra are obtained using
 201 discrete prolate spheroidal sequences (Slepian 1978), characterised by the half-bandwidth
 202 parameter NW , and the number of tapers K which is restricted by $K \leq 2NW - 1$ to reduce
 203 spectral leakage. Smaller values of both K and NW improve the wavenumber-domain
 204 resolution of the resulting power spectra, while higher values of K improve their estimation
 205 variance (Simons *et al.* 2000, 2003). Note that here we use non-italicised notation “ NW ” for
 206 the half-bandwidth parameter; in Section 8.2 we explain how the actual half-bandwidth in
 207 km^{-1} (W) is derived from this.

208

209 First, a power spectrum at taper j , $S_j(\mathbf{k})$, is determined by multiplying the space domain data
 210 by a taper τ_j , and Fourier transforming:

211
$$S_j(\mathbf{k}) = \mathbf{F}_2 \{ g(\mathbf{x}) \tau_j(\mathbf{x}) \} . \quad (12)$$

212 As is customary with 2D data, we form an azimuthal-average power spectrum by averaging

213 $S_j(\mathbf{k})$ over annuli in the wavenumber domain:

214
$$S_j(k) = \frac{1}{N_a} \sum_{i=1}^{N_a} S_j(|\mathbf{k}|_i) , \quad (13)$$

215 where N_a is the number of power estimates in an annulus, and will vary over annuli. The
 216 wavenumber annuli we use have equal spacing in \log_{10} radial wavenumber ($k \equiv |\mathbf{k}|$). The final
 217 multitaper spectrum is then the average of the annular-averaged power over the tapers:

$$218 \quad S(k) = \frac{1}{K^2} \sum_{j=1}^{K^2} S_j(k) , \quad (14)$$

219 since in 2D there are K^2 tapers.

220

221 **4. The Morlet Wavelet**

222 The fan wavelet spectra we study here are obtained from superpositions of 2D Morlet
 223 wavelets. The 2D Morlet wavelet (Dallard & Spedding 1993), can be defined in both space
 224 and wavenumber domains. Furthermore, it has two forms, the simple and complete wavelets.

225

226 The space domain equation of the simple 2D Morlet wavelet is:

$$227 \quad \psi(\mathbf{x}) = e^{i\mathbf{k}_0 \cdot \mathbf{x}} e^{-|\mathbf{x}|^2/2} \quad (15)$$

228 (Dallard & Spedding 1993; Antoine *et al.* 2004), where $|\mathbf{k}_0|$ is the ‘central wavenumber’, and
 229 governs the resolution of the wavelet in the space and wavenumber domains. Larger values of
 230 $|\mathbf{k}_0|$ give better wavenumber resolution but poorer spatial resolution, and vice versa for
 231 smaller values (Addison 2002). This is discussed further in Section 8.1. In the wavenumber
 232 domain the simple 2D Morlet wavelet’s equation is:

$$233 \quad \hat{\psi}(\mathbf{k}) = e^{-|\mathbf{k}-\mathbf{k}_0|^2/2} \quad (16)$$

234 (Dallard & Spedding 1993; Antoine *et al.* 2004).

235

236 However, when $|\mathbf{k}_0|$ is small (generally taken to be $|\mathbf{k}_0| < 5$), the simple Morlet wavelet has a
 237 significant non-zero mean value, which results in it no longer being a true wavelet (Addison

238 2002). Hence a correction is made to restore zero mean, giving the complete Morlet wavelet.

239 The space domain equation of the complete 2D Morlet wavelet is:

$$240 \quad \psi(\mathbf{x}) = \left(e^{i\mathbf{k}_0 \cdot \mathbf{x}} - e^{-|\mathbf{k}_0|^2/2} \right) e^{-|\mathbf{x}|^2/2} \quad (17)$$

241 (Addison *et al.* 2002; Antoine *et al.* 2004). In the wavenumber domain its equation is:

$$242 \quad \hat{\psi}(\mathbf{k}) = e^{-|\mathbf{k}-\mathbf{k}_0|^2/2} - e^{-\left(\mathbf{k}^2+|\mathbf{k}_0|^2\right)/2} \quad (18)$$

243 (Addison *et al.* 2002; Antoine *et al.* 2004). The extra terms present in the complete wavelet's

244 formulae make closed, analytic solutions of some of its properties impossible. Therefore,

245 when we look at the orthogonality properties in Section 6 we use the equations of the simple

246 wavelet, as we do when investigating its bandwidth resolution (Section 8). However, when

247 performing numerical computations we use the complete wavelet, as in its large-scale

248 behaviour (Section 5), and in estimation of fractal data power spectra (Sections 9 and 10).

249

250 In this study we analyse wavelet power spectra using six values of $|\mathbf{k}_0|$. Their choice,

251 described in Kirby & Swain (2011), is governed by the amplitude of the first sidelobes of the

252 simple wavelet. If this amplitude is a fraction $1/p$ ($p > 1$) of the amplitude of the central peak

253 of the real part of the space domain wavelet, then $|\mathbf{k}_0| = \pi\sqrt{2/\ln p}$. The values of $|\mathbf{k}_0|$ that we

254 use in this study are 2.668, 3.081, 3.773, 5.336, 7.547 and 10.673, which give a space domain

255 wavelet whose first sidelobes are $1/16$, $1/8$, $1/4$, $1/2$, $(1/2)^{1/2}$ and $(1/2)^{1/4}$ of the magnitude of

256 the central amplitude, respectively.

257

258 The peak wavenumber of the simple 2D Morlet wavelet at a scale s is given by:

$$259 \quad \kappa = \frac{|\mathbf{k}_0|}{s} \quad (19)$$

260 (Kirby 2005). Kirby & Swain (2011) have given a method to compute the peak wavenumber

261 for the complete version, which has no closed, analytic equation.

262

263 The cone of influence for the simple Morlet wavelet can be derived from eq. (15):

264 $|\mathbf{x}_{coi}| = s \sqrt{-2 \ln q_{coi}} \text{ ,}$ (20)

265 at a scale s . For $q_{coi} = e^{-1}$, the COI is:

266 $|\mathbf{x}_{coi}| = s \sqrt{2} \approx 1.41 s \text{ .}$ (21)

267 In this study we also investigate a COI where the wavelet decays to half its peak amplitude

268 ($q_{coi} = 0.5$), whereby

269 $|\mathbf{x}_{coi}| = s \sqrt{2 \ln 2} \approx 1.18 s \text{ .}$ (22)

270 For now we leave the specific definition of the COI open, and investigate its particular value

271 further in Section 9.4.

272

273 **5. Large-Scale Behaviour**

274 Being a convolution between a signal and a wavelet in the space domain, eq. (1), the CWT is

275 often evaluated in the wavenumber domain using the inverse Fourier transform to decrease

276 computation time, as in eq. (3) (Farge 1992; Torrence & Compo 1998). This is possible

277 because most continuous wavelets can be defined by their wavenumber-domain analytic

278 equations. Space-domain analytic equations for many of these wavelets do not exist because

279 it is not always possible to perform the integration needed to compute the inverse Fourier

280 transform analytically. This, then, is a second reason for use of the wavenumber-domain

281 implementation of the CWT.

282

283 Some wavelets, though, can be defined in both space and wavenumber domains by analytic

284 equations. For these, the CWT may be implemented either by space-domain convolution or

285 wavenumber-domain multiplication. Nevertheless, most studies will still use the Fourier

286 approach because it is faster. Here, we have found that differences exist between wavelets
 287 defined in the space-domain, and their counterparts derived from numerical inverse Fourier
 288 transformation of the wavenumber-domain equations. These differences arise at the very
 289 largest and very smallest wavelet scales, and as we show, are due to the discretisation of the
 290 spatial and wavenumber domains.

291

292 Fig. 1 shows three 2D Morlet wavelets in the wavenumber domain, at azimuths of $\alpha = 0^\circ$, 15°
 293 and 30° , and at two scales. At the largest scale (left-hand panels) the wavenumber domain
 294 grid is not fine enough to register a difference between a wavelet with an azimuth of 0° and
 295 one with 15° , and the two wavelets, when used in the CWT, will give identical wavelet
 296 coefficients, i.e., as though azimuth was 0° . At 30° azimuth the large-scale wavelet is
 297 correctly represented, as are the smaller-scale wavelets (right-hand panels) at all azimuths
 298 because these wavelets are broader functions in the wavenumber domain.

299

300 Fig. 2 shows the effect in the space domain for a wavelet with an azimuth of 10° , and shows
 301 that in order to obtain correct wavelet coefficients, the largest-scale coefficients should be
 302 computed using convolution with the space-domain form of the wavelet, rather than through
 303 the Fourier transform approach (Section 2.1). We determine the scales and azimuths at which
 304 convolution should be performed by computing the normalised energy difference (i.e.,
 305 summed over all space) between the space-domain wavelet, ψ (taken to be the true definition
 306 of the wavelet), and the equivalent defined by inverse Fourier transformation of the
 307 wavenumber domain representation ($\mathbf{F}_2^{-1}[\hat{\psi}]$):

$$308 \quad \Delta E_{i,j} = \frac{\sum_{\mathbf{x}} |\psi_{i,j} - \mathbf{F}_2^{-1}[\hat{\psi}_{i,j}]|^2}{\sum_{\mathbf{x}} |\psi_{i,j}|^2}, \quad (23)$$

309 at a scale index j and azimuth index i . The wavelets ψ and $\mathbf{F}_2^{-1}[\hat{\psi}]$ are both normalised to unit
310 maximum amplitude before implementation of eq. (23). Fig. 3 shows a plot of $\Delta E_{i,j}$ versus
311 scale and azimuth indices, for the 2D Morlet wavelets constituting an isotropic fan. As our
312 threshold, we choose that when $\Delta E_{i,j} > 0.01$ then space-domain convolution should be used,
313 at scale indices less than $N_s/2$; otherwise the speedier Fourier transform method is used. The
314 high values of $\Delta E_{i,j}$ at small scales arise because the space-domain wavelet is too spatially-
315 narrow to be well-defined at the data grid spacing; at such scales the Fourier transform
316 method is used.

317

318 **6. Orthogonality of Morlet Wavelets**

319 The jackknife method of error estimation requires that the signal estimates to be jackknifed
320 are independent (Thomson & Chave 1991). However, because continuous wavelets are non-
321 orthogonal, the wavelet coefficients of a signal will not be independent. Since, in this study,
322 we construct a fan by superposition of 2D Morlet wavelets, we investigate the orthogonality
323 properties of this wavelet in the space-azimuth domain. We show that careful selection of
324 parameters can yield approximate orthogonality, thus minimizing leakage between wavelet
325 coefficients, and ensuring quasi-independence of jackknifed estimates.

326

327 Take two normalised space-domain wavelets at different scales, locations and azimuths ($\psi_{s,t,\alpha}$
328 and $\psi_{a,b,\beta}$), and evaluate what we refer to here as the ‘degree of orthogonality’:

$$329 \quad O_{st\alpha} = \int_{-\infty}^{\infty} \int_{-\infty}^{\infty} \psi_{s,t,\alpha}(\mathbf{x}) \psi_{a,b,\beta}^*(\mathbf{x}) d^2\mathbf{x} . \quad (24)$$

330 For truly orthogonal wavelets it would be true that:

$$331 \quad O_{st\alpha} = \begin{cases} 1 & s = a \text{ and } \mathbf{t} = \mathbf{b} \text{ and } \alpha = \beta \\ 0 & \text{otherwise} \end{cases} , \quad (25)$$

332 but as we shall see for the Morlet wavelet, $0 < |O_{st\alpha}| \leq 1$.

333

334 Here we use the simple Morlet wavelet, because no simple algebraic solutions exist for the
 335 complete wavelet. However, as we note at the end of Section 6, a comparison of results
 336 obtained via the following algebraic approach (on the simple wavelet) with results obtained
 337 by numerical evaluation (using the complete wavelet) showed there to be very little
 338 difference, even when $|\mathbf{k}_0| = 2.668$.

339

340 Choose the two wavelets to have the same central wavenumber $|\mathbf{k}_0|$, where $\mathbf{k}_0 = (k_{x0}, k_{y0}) =$
 341 $|\mathbf{k}_0|(\cos \alpha, \sin \alpha)$, and $\mathbf{l}_0 = (l_{x0}, l_{y0}) = |\mathbf{k}_0|(\cos \beta, \sin \beta)$. First, just consider one of the 2D
 342 wavelets. Here we use the normalisation constant for the 2D Morlet wavelet which can be
 343 shown to be $\pi^{-1/2}$. Letting $\mathbf{x} = (x, y)$ and $\mathbf{t} = (t_x, t_y)$, we have:

$$\begin{aligned}
 \psi_{s,t,\alpha}(\mathbf{x}) &= (s\sqrt{\pi})^{-1} e^{i\mathbf{k}_0 \cdot (\mathbf{x}-\mathbf{t})/s} e^{-|\mathbf{x}-\mathbf{t}|^2/2s^2} \\
 &= (s\sqrt{\pi})^{-1} e^{i[k_{x0}(x-t_x)+k_{y0}(y-t_y)]/s} e^{-[(x-t_x)^2+(y-t_y)^2]/2s^2} \\
 344 &= (s\sqrt{\pi})^{-1/2} e^{ik_{x0}(x-t_x)/s} e^{-(x-t_x)^2/2s^2} (s\sqrt{\pi})^{-1/2} e^{ik_{y0}(y-t_y)/s} e^{-(y-t_y)^2/2s^2} \\
 &= \psi_{s,t_x,\alpha}(x) \psi_{s,t_y,\alpha}(y) .
 \end{aligned} \tag{26}$$

345 That is, the 2D simple Morlet wavelet is the product of two 1D simple Morlet wavelets, or
 346 more accurately, the product of a 1D wavelet with central wavenumber $|\mathbf{k}_0|\cos \alpha$ and one
 347 with central wavenumber $|\mathbf{k}_0|\sin \alpha$.

348

349 Therefore we can separate the x and y components in eq. (24), giving:

$$\begin{aligned}
O_{st\alpha} &= \int_{-\infty}^{\infty} \int_{-\infty}^{\infty} \psi_{s,t_x,\alpha}(x) \psi_{s,t_y,\alpha}(y) \psi_{a,b_x,\beta}^*(x) \psi_{a,b_y,\beta}^*(y) dx dy \\
350 \quad &= \left(\int_{-\infty}^{\infty} \psi_{s,t_x,\alpha}(x) \psi_{a,b_x,\beta}^*(x) dx \right) \left(\int_{-\infty}^{\infty} \psi_{s,t_y,\alpha}(y) \psi_{a,b_y,\beta}^*(y) dy \right) \\
&= I_x I_y .
\end{aligned} \tag{27}$$

351 So, taking only the x -direction wavelets (the integrand of I_x):

$$\begin{aligned}
352 \quad \psi_{s,t_x,\alpha}(x) \psi_{a,b_x,\beta}^*(x) &= \left(s\sqrt{\pi} \right)^{-1/2} e^{ik_{x0}(x-t_x)/s} e^{-(x-t_x)^2/2s^2} \left(a\sqrt{\pi} \right)^{-1/2} e^{-il_{x0}(x-b_x)/a} e^{-(x-b_x)^2/2a^2} \\
&= A e^{-Bx^2+(C+iD)x} ,
\end{aligned} \tag{28}$$

353 where

$$354 \quad A = (\pi sa)^{-1/2} e^{i(l_{x0}b_x/a - k_{x0}t_x/s)} e^{-(t_x^2/s^2 + b_x^2/a^2)/2} , \tag{29}$$

$$355 \quad B = (s^{-2} + a^{-2})/2 , \tag{30}$$

$$356 \quad C = t_x s^{-2} + b_x a^{-2} , \tag{31}$$

$$357 \quad D = k_{x0} s^{-1} - l_{x0} a^{-1} . \tag{32}$$

358 Therefore

$$359 \quad I_x = A \int_{-\infty}^{\infty} e^{-Bx^2+(C+iD)x} dx = A\sqrt{\pi B^{-1}} e^{(C+iD)^2/4B} \tag{33}$$

360 (Abramowitz 1972). Substituting eqs (29) – (32) into eq. (33) we find:

$$361 \quad I_x = \sqrt{\frac{2sa}{s^2 + a^2}} e^{-[(t_x - b_x)^2 + (s l_{x0} - a k_{x0})^2]/2(s^2 + a^2)} e^{i(b_x - t_x)(s k_{x0} + a l_{x0})/(s^2 + a^2)} . \tag{34}$$

362 The equation for I_y is similar, giving, from eq. (27):

$$363 \quad O_{st\alpha} = \frac{2sa}{s^2 + a^2} e^{-[|\mathbf{b} - \mathbf{t}|^2 + |s\mathbf{l}_0 - a\mathbf{k}_0|^2]/2(s^2 + a^2)} e^{i(\mathbf{s}\mathbf{k}_0 + a\mathbf{l}_0) \cdot (\mathbf{b} - \mathbf{t})/(s^2 + a^2)} . \tag{35}$$

364 Note that if $a = s$, $\mathbf{b} = \mathbf{t}$, and $\beta = \alpha$, then $O_{st\alpha} = 1$ and is real-valued. Note also that, for $a \neq s$,

365 $\mathbf{b} \neq \mathbf{t}$, and $\beta \neq \alpha$, $O_{st\alpha}$ is complex-valued, and $|O_{st\alpha}| > 0$, showing that Morlet wavelets are

366 non-orthogonal.

367

368 In the following analysis we will study only the modulus of eq. (35), $|O_{st\alpha}|$, and ignore the
 369 complex exponential term which merely provides oscillations, but we note that when the two
 370 wavelets have the same spatial location ($\mathbf{t} = \mathbf{b}$) this complex exponential disappears and eq.
 371 (35) is real-valued.

372

373 Since the jackknife will not be performed over scale, we can take the two wavelets to be at
 374 the same scale, $s = a$, and eq. (35) becomes the space-azimuth orthogonality:

$$375 \quad |O_{t\alpha}| = e^{-|\mathbf{b}-\mathbf{t}|^2/4s^2} e^{-|\mathbf{k}_0-\mathbf{k}|^2/4} . \quad (36)$$

376 Letting $\Delta x = b_x - t_x$ and $\Delta y = b_y - t_y$, so that $|\mathbf{b} - \mathbf{t}|^2 = \Delta x^2 + \Delta y^2$, and defining a scale-
 377 normalised distance between wavelets, $\xi = s^{-1}(\Delta x^2 + \Delta y^2)^{1/2}$, eq. (36) becomes:

$$378 \quad |O_{t\alpha}| = e^{-\xi^2/4} e^{-|\mathbf{k}_0|^2 \sin^2(\delta\alpha/2)} , \quad (37)$$

379 where we have let the two wavelets be separated by a rotation $\delta\alpha = \beta - \alpha$, and have used the
 380 identity $1 - \cos 2\phi = 2\sin^2 \phi$ for an arbitrary angle ϕ .

381

382 It can be seen in eq. (37) that $|O_{t\alpha}|$ is strongly dependent upon the value of $|\mathbf{k}_0|$. This is to be
 383 expected as smaller $|\mathbf{k}_0|$ values result in broader wavelets in \mathbf{k} -space, meaning that their
 384 angular separation must be larger in order to maintain a low value of $|O_{t\alpha}|$.

385

386 We thus desire a new parameter representing angular separation that makes $|O_{t\alpha}|$ independent
 387 of, or weakly-dependent on, $|\mathbf{k}_0|$. Take the 2D simple Morlet daughter wavelet in the
 388 wavenumber domain, eq. (16), in polar coordinates (k, θ) :

$$389 \quad \hat{\psi}_{s,\alpha}(k, \theta) = s e^{-[s^2 k^2 + |\mathbf{k}_0|^2 - 2s|\mathbf{k}_0|k \cos(\theta - \alpha)]/2} , \quad (38)$$

390 where $k \equiv |\mathbf{k}|$, and evaluate at $\alpha = 0^\circ$ and the peak wavenumber $k = \kappa = |\mathbf{k}_0|/s$:

391 $\hat{\psi}_{s,\alpha}(k, \theta) = s e^{-|\mathbf{k}_0|^2(1-\cos\theta)}$. (39)

392 At some $\theta = \theta_{q_\alpha}$ the wavelet has a value of q_α ($0 < q_\alpha < 1$) times its maximum value (which
 393 is s). We refer to q_α as the ‘azimuthal overlap parameter’. Thus:

394 $e^{-|\mathbf{k}_0|^2(1-\cos\theta_{q_\alpha})} = q_\alpha$. (40)

395 Since the angular separation between adjacent wavelets overlapping at θ_{q_α} is $\delta\alpha = 2\theta_{q_\alpha}$,

396 solving eq. (40) we get:

397 $\delta\alpha = 2 \cos^{-1}\left(1 + |\mathbf{k}_0|^{-2} \ln q_\alpha\right)$, (41)

398 which is independent of scale. Now, using the identity $\cos(2 \cos^{-1} x) = 2x^2 - 1$ (Abramowitz

399 1972), and the relationship $2 \sin^2(\phi/2) = 1 - \cos \phi$, we find:

400 $\sin^2(\delta\alpha/2) = -|\mathbf{k}_0|^{-2} \ln q_\alpha \left(2 + |\mathbf{k}_0|^{-2} \ln q_\alpha\right)$. (42)

401 So, substituting eq. (42) into eq. (37) gives:

402 $|O_{t_\alpha}| = e^{-\xi^2/4} q_\alpha^{2 + |\mathbf{k}_0|^{-2} \ln q_\alpha}$. (43)

403 Eq. (43) is plotted in Fig. 4. It shows that, when expressed as a function of q_α , the space-
 404 azimuth orthogonality is only very weakly dependent upon $|\mathbf{k}_0|$ for two wavelets at the same
 405 scale.

406

407 Fig. 4 shows that two spatially-close wavelets (low ξ) at the same scale can still exhibit
 408 approximate orthogonality if their azimuths are chosen carefully. Furthermore, when two
 409 wavelets have an azimuth separation corresponding to $q_\alpha \approx 0.3$, even spatially-coincident
 410 wavelets ($\xi = 0$) have a space/azimuth-orthogonality of approximately 0.1 at any $|\mathbf{k}_0|$ value.

411 Using a mathematically-elegant value of $q_\alpha = e^{-1} \approx 0.368$ in eq. (43) and rearranging, we get:

412 $\xi = 2\sqrt{|\mathbf{k}_0|^{-2} - 2 - \ln|O_{t_\alpha}|}$. (44)

413 Thus, if we desire $|O_{t\alpha}| < 0.1$, then the distance/scale separation may be chosen as low as $\xi =$
414 1.33 for $|\mathbf{k}_0| = 2.668$, or $\xi = 1.12$ for $|\mathbf{k}_0| = 10.673$, when $q_\alpha = e^{-1}$.

415

416 Fig. 4 and eq. (43) also show that when two wavelets have the same azimuth ($q_\alpha = 1$), in
417 order to achieve $|O_{t\alpha}| < 0.1$ they must be separated by a distance/scale ratio of $\xi \approx 3$, which is
418 approximately twice the e -folding distance for the Morlet wavelet, $2s\sqrt{2}$, at a scale s , eq. (21).

419

420 As a final note, we can report that a numerical evaluation of eq. (43) gave visually identical
421 results to those presented in Fig. 4. This was even true for complete Morlet wavelets, which
422 differ from the simple wavelet when $|\mathbf{k}_0|$ is low, showing that the corrections for non-zero
423 mean do not significantly change the orthogonality properties of the wavelet.

424

425 **7. Jackknife Errors**

426 **7.1 Multitaper method**

427 When applied to the multitaper method, jackknife error estimates of the power spectrum are
428 obtained by performing the jackknife over the power estimates from each taper (Thomson
429 2007). Although Slepian tapers are orthogonal, the power estimates at each taper are only
430 approximately independent on a grid in the wavenumber domain. However, we take this to
431 satisfy the requirement of the jackknife method that the signal estimates to be jackknifed are
432 independent (Thomson & Chave 1991). Note that error estimates cannot be determined when
433 a single taper is used.

434

435 The jackknifed errors are obtained as follows (Thomson 2007). Form a “delete-one”
436 spectrum estimate by averaging the power over all tapers except one:

437
$$S_{\setminus j}(k) = \frac{1}{K^2 - 1} \sum_{\substack{i=1 \\ i \neq j}}^{K^2} S_i(k) . \quad (45)$$

438 The mean of all the delete-one estimates is then taken:

439
$$S_{\setminus \bullet}(k) = \frac{1}{K^2} \sum_{j=1}^{K^2} S_{\setminus j}(k) . \quad (46)$$

440 The jackknife variance is then computed through:

441
$$\text{var}[S](k) = \frac{K^2 - 1}{K^2} \sum_{j=1}^{K^2} [S_{\setminus j}(k) - S_{\setminus \bullet}(k)]^2 \quad (47)$$

442 (Thomson & Chave 1991; Thomson 2007), and the jackknife error as:

443
$$\sigma_M(k) = \sqrt{\text{var}[S](k)} . \quad (48)$$

444

445 **7.2 Local wavelet error spectra**

446 In the new method to compute jackknife errors on local wavelet power spectra for the fan
 447 wavelet transform, we follow the procedure for the multitaper method, but jackknife over
 448 azimuths instead of over tapers. Thus the jackknife is performed on power spectra at each
 449 azimuth in the fan, $|\tilde{g}(s, \mathbf{x}, \alpha)|^2$ from eq. (8), giving error estimates at each space domain
 450 point, \mathbf{x} , and scale, s . From the orthogonality studies of Section 6, approximate independence
 451 of the jackknifed estimates is satisfied when the Morlet wavelets in the fan are separated by
 452 an azimuthal overlap parameter of $q_\alpha = e^{-1}$.

453

454 Let $P(s, \mathbf{x}, \alpha_i)$ be the local scalogram at scale s , spatial location \mathbf{x} and azimuth α_i , as in eq. (8).

455 The total number of azimuths is N_α which is the total number of independent local power
 456 estimates at that scale and location. Form a “delete-one” spectrum estimate by averaging the
 457 power over all azimuths except one:

458
$$P_{\setminus j}(s, \mathbf{x}) = \frac{1}{N_\alpha - 1} \sum_{\substack{i=1 \\ i \neq j}}^{N_\alpha} P(s, \mathbf{x}, \alpha_i) , \quad (49)$$

459 similarly to Thomson (2007) for the MT method. We then take the mean of all the delete-one
 460 estimates:

461
$$P_{\setminus \bullet}(s, \mathbf{x}) = \frac{1}{N_\alpha} \sum_{j=1}^{N_\alpha} P_{\setminus j}(s, \mathbf{x}) . \quad (50)$$

462 The jackknife variance of the delete-one scalogram estimates is thus:

463
$$\text{var}[P](s, \mathbf{x}) = \frac{N_\alpha - 1}{N_\alpha} \sum_{j=1}^{N_\alpha} [P_{\setminus j}(s, \mathbf{x}) - P_{\setminus \bullet}(s, \mathbf{x})]^2 \quad (51)$$

464 The local jackknifed error spectra are then given by the standard deviation:

465
$$\sigma_w(s, \mathbf{x}) = \sqrt{\text{var}[P](s, \mathbf{x})} . \quad (52)$$

466

467 **7.3 Global wavelet error spectra**

468 The above method can be adapted to provide error estimates on the global wavelet power
 469 spectrum. However, when two wavelets have equal azimuth but are at different spatial
 470 locations, adjacent local scalogram estimates in the space domain are not independent, and
 471 only become (almost) independent when the distance between wavelets is approximately
 472 $\geq 2s\sqrt{2}$ for a scale s (Section 6). Therefore we implement a scheme to average the power
 473 estimates at a given azimuth over spatial blocks of size $2s\sqrt{2}$, assume these blocks to have
 474 independence of power, and then form the delete-one estimates over the averaged blocks at
 475 each azimuth.

476

477 Let $\bar{P}_m(s, \bar{\mathbf{x}}, \alpha)$ be the m^{th} spatially-averaged local scalogram at scale s , averaged spatial block
 478 $\bar{\mathbf{x}}_n$ and azimuth α_j , where m is a unique identifier of j and n . The total number of space-
 479 domain blocks is $N_{\bar{\mathbf{x}}}N_{\bar{\mathbf{y}}}$; the total number of azimuths is N_α ; therefore the total number of

480 independent local power estimates is $M = N_{\bar{x}}N_{\bar{y}}N_{\alpha}$. Form a “delete-one” spectrum estimate
 481 by averaging the power over all azimuths and spatial blocks except one:

$$482 \quad P_{\setminus m}(s, \bar{\mathbf{x}}) = \frac{1}{M-1} \sum_{\substack{i=1 \\ i \neq m}}^M \bar{P}_i(s, \bar{\mathbf{x}}, \alpha) . \quad (53)$$

483 We then take the mean of all the delete-one estimates:

$$484 \quad P_{\setminus \bullet}(s) = \frac{1}{M} \sum_{m=1}^M P_{\setminus m}(s, \bar{\mathbf{x}}) . \quad (54)$$

485 The jackknife variance of the delete-one scalogram estimates is thus:

$$486 \quad \text{var}[P](s) = \frac{M-1}{M} \sum_{m=1}^M [P_{\setminus m}(s, \bar{\mathbf{x}}) - P_{\setminus \bullet}(s)]^2 . \quad (55)$$

487 The global jackknifed error spectra are then given by the standard deviation:

$$488 \quad \sigma_w(s) = \sqrt{\text{var}[P](s)} . \quad (56)$$

489 Note that at the largest scales the block size $2s\sqrt{2}$ will be greater than half the data length. At
 490 such scales we have $N_{\bar{x}} = N_{\bar{y}} = 1$, but we also have $N_{\alpha} > 1$ so can still form meaningful
 491 variances.

492

493 **8. Wavenumber Resolution**

494 **8.1 Morlet wavelets**

495 As well as determining an error on the power spectrum, it is also instructive to estimate the
 496 uncertainty on the wavenumber, via the bandwidth. For the 2D simple Morlet wavelet, we
 497 can readily derive an analytic expression for its bandwidth about the peak wavenumber, eq.
 498 (19). In polar coordinates (k, θ) , eq. (16) becomes:

$$499 \quad \hat{\psi}_{s,\alpha}(k, \theta) = s e^{-\left[s^2 k^2 - 2sk|\mathbf{k}_0|\cos(\theta-\alpha) + |\mathbf{k}_0|^2\right]/2} , \quad (57)$$

500 for the simple wavelet. Since the wavelet is rotationally-symmetric in the wavenumber
 501 domain about its peak, evaluate this equation along a locus of $\theta = \alpha$:

502 $\hat{\psi}_{s,\alpha}(k, \alpha) = s e^{-(sk - |\mathbf{k}_0|)^2/2}$. (58)

503 The maximum value of $\hat{\psi}$ is s , so the wavelet has a fraction q ($0 < q < 1$) of this maximum at
 504 some wavenumber $k = k_q$:

505 $e^{-(sk_q - |\mathbf{k}_0|)^2/2} = q$, (59)

506 giving:

507 $k_q = \frac{|\mathbf{k}_0|}{s} \pm \frac{\sqrt{-2 \ln q}}{s}$. (60)

508 Thus the half-bandwidth at some scale s is:

509 $\Delta_{\hat{\psi}}(s) = \frac{\sqrt{-2 \ln q}}{s}$. (61)

510 Alternatively we can express the half-bandwidth in term of the equivalent Fourier
 511 wavenumber. Representing this by the peak wavenumber, we substitute eq. (19), giving:

512 $\Delta_{\hat{\psi}}(\kappa) = \kappa \frac{\sqrt{2 \ln 2}}{|\mathbf{k}_0|}$, (62)

513 where we now define the wavenumber resolution as being the half-width of the wavelet at its
 514 half-amplitude, i.e. with $q = 0.5$. Eq. (62) hence gives the bandwidth resolution of the 2D
 515 Morlet wavelet at some wavenumber κ . Since there is no simple analytic solution for
 516 complete Morlet wavelets, eq. (62) is only approximate for wavelets with $|\mathbf{k}_0| < 5$, though see
 517 Kirby & Swain (2011) for an expanded discussion. Fig. 5a illustrates the concept of wavelet
 518 bandwidth.

519

520 It can be seen that the bandwidth varies linearly with wavenumber. That is, 2D Morlet
 521 wavelets have better wavenumber resolution at low wavenumbers than at large ones. The
 522 bandwidth is also inversely proportional to $|\mathbf{k}_0|$, with high values of this parameter giving

523 better wavenumber resolution. Fig. 6 shows plots of the half-bandwidth of Morlet wavelets,
524 from eq. (62), for various $|\mathbf{k}_0|$.

525

526 **8.2 Slepian tapers**

527 The wavenumber-dependence of the wavenumber resolution is a property of the wavelet
528 transform not exhibited by the MT method (Addison 2002), which, for a given data size, has
529 a fixed resolution at all wavenumbers determined by the NW parameter. The half-bandwidth
530 (W) in the MT method is obtained from the NW parameter by noting that $NW = NW\Delta x$ (note
531 italics), where Δx is the signal grid spacing, and N is the number of observations. Taking L as
532 the length of the signal, $L = N\Delta x$, we can write the half-bandwidth of the multitaper method
533 as:

$$534 \quad W = 2\pi \frac{NW}{L} \quad (63)$$

535 (Simons *et al.* 2000). The factor of 2π reflects our use of rad km^{-1} for wavenumber units,
536 rather than km^{-1} . As noted, the wavenumber resolution is wavenumber-independent, and is
537 proportional to NW, and inversely proportional to the data length. Thus, small values of NW
538 give better wavenumber resolution.

539

540 Fig. 5b illustrates the concept of bandwidth for Slepian tapers. Fig. 6 shows values of the
541 half-bandwidth of Slepian tapers, from eq. (63), for various NW with $L = 5100$ km, this being
542 the length of one side of the area of the fractal surfaces we use.

543

544 **9. Application to Fractal Data Sets**

545 **9.1 Data generation**

546 In this section we compute the spectra of 2D signals with a red spectrum (i.e., high power at

547 long wavelengths, low power at short wavelengths) because our investigation primarily
548 concerns long-wavelength spectrum and error estimation. Specifically we choose signals with
549 a fractal spectrum since these occur frequently in the geosciences (e.g., Turcotte 1997). We
550 compute global spectra and error spectra from the fan wavelet transform and, as comparison,
551 from the multitaper method.

552

553 We generated 100 fractal surfaces using the SpectralSynthesisFM2D algorithm of Saupe
554 (1988). Each surface had fractal dimension 2.5 and was formed from a different random seed,
555 with normally-distributed amplitudes and random phases. The surfaces are hence stationary,
556 which is desired for this study of global spectra. The surfaces were created on a 256×256
557 node Cartesian grid with a 20 km spacing, with each surface having a variance of 10^4 .

558

559 Owing to the nature of the SpectralSynthesisFM2D algorithm, each of these 100 surfaces is
560 periodic. Therefore, to simulate non-periodic surfaces, as would occur in nature, we created a
561 further set of 100 surfaces by extracting the central 256×256 grid nodes from 100 512×512
562 size surfaces also generated using SpectralSynthesisFM2D on a 20 km grid. These extracted
563 non-periodic surfaces were also assigned a variance of 10^4 .

564

565 **9.2 Spectral estimation**

566 The spectra and errors of each surface were computed using different values of NW and K in
567 the MT method, and different values of $|\mathbf{k}_0|$ for the fan-WT. Whereas multitaper spectra give
568 the (annular-averaged) power for the whole data set, wavelet spectra come in various forms.
569 Fig. 7a shows a slice through the scalogram for a single fractal model, $P(s, \mathbf{x})$ from eq. (9),
570 and Fig. 7b the corresponding jackknifed error along the slice, $\sigma(s, \mathbf{x})$ from eq. (52). These
571 images show the spatial variation of power (and its error), whereas Fig. 7c shows the power

572 and error bounds at just one location. In contrast, Fig. 7d shows the global power spectrum,
573 from eq. (11), and global error from eq. (56), for this fractal model. The smaller errors in the
574 global case at higher wavenumbers, compared to the local case, is a consequence of there
575 being more independent power estimates at smaller scales (higher equivalent Fourier
576 wavenumbers) in the global spectrum.

577

578 As can be seen in Fig. 7d, the observed global power spectrum departs from the theoretical
579 expectation for the fractal model. This occurs due to the random nature of the surface
580 generation. In order to reduce these random effects, we took the arithmetic means of the 100
581 spectra and errors and did this for each analysis method. For example, a more representative
582 global power spectrum can be obtained by taking the average of 100 versions of Fig. 7d.

583

584 **9.3 Periodic data**

585 Fig. 8 shows that as the bandwidth parameter, NW , and/or the number of tapers, K , are
586 increased, the multitaper-derived spectra are biased at the lower wavenumbers. This bias,
587 which was also noted by Wieczorek & Simons (2005), manifests as a flattening of the
588 spectrum which results in the power at the smallest wavenumbers being reduced, while the
589 power at slightly higher wavenumbers is artificially increased. This is to be expected since
590 higher- NW tapers have a poor low-wavenumber resolution (Section 8.2). However, Fig. 9
591 shows that the wavenumber error bars include the theoretical fractal power spectrum at all
592 wavenumbers.

593

594 Fig. 10 shows that the power recovered by the high- $|\mathbf{k}_0|$ fan wavelet transform has a very
595 good fit to the theoretical power, while the low- $|\mathbf{k}_0|$ wavelets give a consistent upward bias at
596 the mid-to-high wavenumbers. This feature, discussed in Kirby & Swain (2011), arises due to

597 the poorer wavenumber-domain resolution of low- $|\mathbf{k}_0|$ wavelets, but we note that Fig. 9 shows
598 that the theoretical spectrum is still within the errors.

599

600 Importantly, comparison of Figs 8 and 10 shows that the fan-WT errors are generally similar
601 to those of the MT, with both exhibiting a more rapid decrease with wavenumber than the
602 power spectra. We take this as a validation of the new wavelet jackknifing method. It can also
603 be seen in Fig. 8 that the higher-order tapers give reduced error, which is to be expected since
604 the estimation variance of the MT power spectrum improves with increasing K , as $1/K$
605 (Simons *et al.* 2000, 2003).

606

607 Fig. 11 shows only the jackknife errors for periodic data, and in keeping with the long-
608 wavelength subject of this research, we focus discussion upon the smallest wavenumbers.
609 Recall from Section 8 that better bandwidth resolution is provided by tapers with low values
610 of NW , and wavelets with high values of $|\mathbf{k}_0|$. Now Fig. 11a-c shows that the low- NW tapers
611 give the largest power spectral errors. In contrast, Fig. 11d shows that high- $|\mathbf{k}_0|$ wavelets give
612 the smallest power spectral errors. This demonstrates an important difference between
613 wavelet and multitaper methods. In the MT method the smallest long-wavelength errors are
614 achieved using high values of the bandwidth parameter, NW , though these then give a poor
615 wavenumber-domain resolution. Contrastingly for wavelets, the smallest long-wavelength
616 errors are achieved using high values of the $|\mathbf{k}_0|$ parameter which then also provide a good
617 wavenumber-domain resolution.

618

619 **9.4 Non-periodic data**

620 When data are non-periodic, use of the Fourier transform can generate edge effects which
621 will bias spectra. However, since the tapers in the MT method decay to approximately zero at

622 the edges, edge effects should be minimised. Comparison of Figs 8 and 12 shows that the MT
623 method gives a slightly reduced power for the non-periodic data. With just one taper, this
624 power reduction is evident across all wavenumbers; for higher-order tapers the power
625 reduction is manifest at progressively higher wavenumbers only.

626

627 With the wavelet transform, the edge effects should be more pronounced, though this would
628 depend upon the wavelet scale, with the edge effect penetrating further into the scalograms as
629 scale increases and the wavelet broadens spatially. This is seen in Fig. 13 (left panels), which
630 shows the averages of 100 local scalograms of non-periodic data from two $|\mathbf{k}_0|$ values, with
631 their e^{-1} and half-amplitude COIs shown (Section 4). Edge effects are clearly visible at the
632 higher wavenumbers which would bias global spectra. It can also be seen that both cones of
633 influence remove the edge effects, but that the e^{-1} COI is perhaps rather wasteful in the
634 amount of data it omits. Certainly, for stationary data such as these, the half-amplitude COI
635 removes enough edge-affected data to provide reliable global spectra.

636

637 However, both cones remove useful low-wavenumber data. We therefore implemented an
638 extension to the COI of the four central spatial nodes, from the apex of the cone to the
639 smallest wavenumber, shown in Fig. 13. This enabled us to plot global power spectra at the
640 lowest wavenumbers, shown in Fig. 14. Since the data are stationary, the recovered power is
641 unbiased at these low wavenumbers. For non-stationary data we argue that such a scheme
642 could also be implemented, and we test this in Section 11.

643

644 **10. Application to Filtered Data**

645 In order to test the wavenumber-domain resolution of the multitaper and wavelet methods, we
646 took the 200 surfaces and frequency-filtered those using a cosine function which suppressed

647 harmonics between 1000 and 2000 km wavelength (the “block-band”, shown in grey in Figs
648 8, 10, 12 and 14).

649

650 As shown in Figs 8 and 12, the high wavenumber-resolution tapers (low NW, low K) recover
651 the suppressed harmonics of the block-band very well, for both periodic and non-periodic
652 data. However, Fig. 8 also shows that as NW increases, the power of the filtered surfaces in
653 the block-band increases and the wavenumber limits of the recovered block-band migrate to
654 higher wavenumbers. This observation also holds when K is increased, until at high NW and
655 K the unfiltered and filtered spectra are almost indistinguishable.

656

657 The fan-WT does not suffer as much from such block-band migration, even for low- $|\mathbf{k}_0|$
658 wavelets (Figs 10 and 14), though the high power in the block-band is still in evidence at low
659 $|\mathbf{k}_0|$. Note that extension of the COI as described above has resulted in the preservation of
660 useful information about the filtered block-band at low wavenumbers (Figs 13 and 14),
661 whereas strict application of the COI would remove these wavenumbers.

662

663 **11. Application to Real Data: the Congo Basin Gravity Anomaly**

664 We have chosen to test the methods described in this paper on the free air gravity anomaly
665 data over central Africa where a dominant long-wavelength low (Fig. 15) occurs over the
666 Congo basin. Our data were computed from the EGM2008 gravity model to degree and order
667 1000 (Pavlis *et al.* 2012) and gridded using a Mercator projection.

668

669 The local scalograms across the middle of the Congo basin in Fig. 16 reveal the spatial and
670 wavenumber extent of the dominant long-wavelength low in the data (blue colours at smallest
671 wavenumbers). Recall that low- $|\mathbf{k}_0|$ wavelets have good spatial but poor wavenumber

672 resolution, while high- $|\mathbf{k}_0|$ wavelets have good wavenumber but poor spatial resolution
673 (Section 4), so the spatial extent of the low is seen most clearly at low $|\mathbf{k}_0|$. Fig. 16 also shows
674 the varying size of the cone of influence for each $|\mathbf{k}_0|$, and shows how our extension of the
675 COI to low wavenumbers is warranted. At low wavenumbers, the spatial variation of power
676 is small for high- $|\mathbf{k}_0|$ wavelets for the reason stated above, so choosing just the central spatial
677 nodes as representative of the whole is not unreasonable. With the low- $|\mathbf{k}_0|$ wavelets the COI
678 is large enough to include these data without extension.

679

680 Fig. 17 shows global wavelet power spectra (in red) for the 3000 km square area shown in
681 Fig. 15, calculated as for Fig. 14. We have added (in black) the global spectra for the whole
682 area shown in Fig. 15 (~9000 km square) which are in general very smoothly varying, so as
683 to highlight the anomalous positive power anomaly in the smaller area at the lower
684 wavenumbers ($<0.013 \text{ rad km}^{-1}$, i.e. $>500 \text{ km}$ wavelength). The power anomaly is clearly
685 visible at all values of $|\mathbf{k}_0|$. The power begins to rise at $\sim 6 \times 10^{-3} \text{ rad km}^{-1}$ (1000 km
686 wavelength), reaching a peak at $\sim 3 \times 10^{-3} \text{ rad km}^{-1}$ (2000 km wavelength); the spectrum ends
687 at $\sim 2 \times 10^{-3} \text{ rad km}^{-1}$ (3000 km wavelength) and the maximum wavelength of the anomalous
688 power is not seen. The spectral range of this anomaly (1000 to $>3000 \text{ km}$) is much larger than
689 that of the anomaly in the filtered synthetic model data (1000–2000 km) shown in Figs 8, 10,
690 12 and 14. Fig. 17 also shows that at the intermediate wavenumbers of approximately 6×10^{-3}
691 rad km^{-1} to $12 \times 10^{-3} \text{ rad km}^{-1}$ (or wavelengths of $\sim 1000\text{--}500 \text{ km}$) the spectral power is lower
692 than in the rest of Africa.

693

694 Downey & Gurnis (2009) used spherical cap “wavelets” (Simons *et al.* 1997) to analyse this
695 anomaly and found it confined to the waveband $\sim 900\text{--}3800 \text{ km}$, peaking at $\sim 1600 \text{ km}$.

696 Bearing in mind the differences in analysis tools (spherical cap “wavelets” vs Cartesian

697 Morlet-fan wavelets) and quantity displayed (RMS gravity anomaly vs wavelet power
698 spectra), we consider the agreement between the two studies to be reasonable. Downey &
699 Gurnis (2009) also present a band-reject gravity image of anomalies with wavelengths
700 between 360 and 900 km which shows smaller amplitude anomalies in central Africa than
701 elsewhere in the continent, in agreement with Fig. 17.

702

703 The multitaper equivalents of Fig. 17 are shown in Fig. 18. As for the filtered data in Fig. 12,
704 the best agreement with the wavelet spectra are for the lowest NW and K values, which give
705 the best wavenumber-resolution. For a given K , the wavenumber limits of the Congo basin
706 anomaly migrate to successively higher wavenumbers as NW increases. And as K increases,
707 the amplitude of the positive power anomaly gets smaller, either to virtually disappear at
708 certain values (e.g., NW = 3, K = 5), or to flatten (e.g., NW = 7, K = 7).

709

710 Fig. 19 shows the same spectra as in Fig. 17 but computed using the Fourier, rather than
711 convolution, method of wavelet transformation. Comparison of these two figures shows that
712 at high values of $|\mathbf{k}_0|$ the Fourier method fails to resolve the positive power anomaly, and that
713 convolution gives spectra with much smoother power variation at the lowest wavenumbers.

714

715 **12. Conclusions**

716 We have developed a method to provide jackknife error estimates on local and global wavelet
717 power spectra. While the local method can be applied strictly to only the fan-WT (because
718 the delete-one estimates are performed over wavelet azimuth), the global method is readily
719 adaptable to any wavelet transform (even in 1D) because the jackknifing is performed over
720 the spatial coordinate as well as azimuth.

721

722 When tested on fractal surfaces, the global wavelet error spectra were shown to agree very
723 well with jackknifed multitaper error estimates, both decreasing with wavenumber at a faster
724 rate than the data spectra. Importantly, we found that Morlet wavelets with a high resolution
725 in the wavenumber domain also provide the smallest power spectrum errors. This finding is
726 in contrast to the multitaper method, in which tapers with the highest wavenumber-domain
727 resolution provide larger spectrum errors than do tapers with a comparatively poor
728 wavenumber resolution.

729

730 Furthermore, the wavenumber-dependence of the wavenumber-domain resolution of wavelets
731 leads to better reproduction of the low-wavenumber part of the spectrum than is provided by
732 the multitaper method when high-order tapers are used, though this depends on the data
733 length.

734

735 As a consequence of this study we have provided formulae for the calculation of the degree
736 of orthogonality of 2D Morlet wavelets in the space-azimuth domain. Azimuthally-adjacent
737 wavelets overlapping at an amplitude of e^{-1} give reasonable orthogonality ($\sim 10\%$) while still
738 providing good azimuthally-averaged power spectra. This improves upon the suggested value
739 for Morlet wavelet superposition of 0.75 (Kirby 2005) which was derived to give a
740 minimum-curvature superposition, but which offers too much redundancy in azimuth. In the
741 space-domain, 10% orthogonality can be achieved when two wavelets of the same azimuth
742 are separated by a distance of $2s\sqrt{2}$, for a scale s ; when they have different azimuths this
743 spatial separation can decrease to $2s\sqrt{\ln 2}$.

744

745 Significantly, we have also found that, at large scales, the CWT is best performed by
746 convolution in the space domain, rather than multiplication in the Fourier domain, because in

747 practice large-scale wavelets are not accurately defined by their wavenumber domain
748 equations. While space-domain convolution is possible for the Morlet wavelet, it would not
749 be for other 2D wavelets for which only a wavenumber-domain equation exists.

750

751 Furthermore, we recommend use of a cone of influence when computing global wavelet
752 power spectra, though we have found that, at least for stationary data, most implementations of
753 the cone are too conservative and can be safely extended to the largest scales.

754

755 Finally, we tested the method on real free air gravity anomaly data over the Congo basin in
756 Africa, which are thus non-stationary and non-periodic. The wavelet method (with a cone of
757 influence applied) successfully resolved the power anomaly of this region, whereas only low-
758 NW and low- K tapers were able to do so. This study also showed the benefit of using space-
759 domain convolution when computing the CWT at large scales.

760

761 **Acknowledgements**

762 We thank Frederik Simons for some discussion, and the three anonymous reviewers and
763 editor for their comments. This study was funded by ARC grant number DP0878453, and is
764 TIGeR publication number 444. Computations were performed on the epic supercomputer,
765 supported by iVEC through the use of advanced computing resources located at
766 <http://ivec.org>.

767

768

769 **References**

770 Abramowitz, M. & Stegun, I.A., 1972. *Handbook of Mathematical Functions*, Dover, New
771 York.

772 Addison, P.S., 2002. *The Illustrated Wavelet Transform Handbook*, Institute of Physics
773 Publishing, Bristol, UK.

774 Addison, P.S., Watson, J.N. & Feng, T., 2002. Low-oscillation complex wavelets, *J. Sound*
775 *Vibr.*, **254**, 733-762.

776 Antoine, J.-P., Murenzi, R., Vandergheynst, P. & Ali, S.T., 2004. *Two-dimensional Wavelets*
777 *and their Relatives*, Cambridge University Press, Cambridge.

778 Audet, P. & Mareschal, J.-C., 2007. Wavelet analysis of the coherence between Bouguer
779 gravity and topography: application to the elastic thickness anisotropy in the Canadian
780 Shield, *Geophys. J. Int.*, **168**, 287-298.

781 Banks, R.J., Francis, S.C. & Hipkin, R.G., 2001. Effects of loads in the upper crust on
782 estimates of the elastic thickness of the lithosphere, *Geophys. J. Int.*, **145**, 291-299.

783 Bloomfield, D.S., McAteer, R.T.J., Lites, B.W., Judge, P.G., Mathioudakis, M. & Keenan,
784 F.P., 2004. Wavelet phase coherence analysis: application to a quiet-sun magnetic
785 element, *Astrophys. J.*, **617**, 623-632.

786 Cazelles, B., Chavez, M., de Magny, G.C., Guegan, J.-F. & Hales, S., 2007. Time-dependent
787 spectral analysis of epidemiological time-series with wavelets, *J. R. Soc. Interface*, **4**, 625-
788 636.

789 Chui, C.K., 1992. *An Introduction to Wavelets*, Academic Press, San Diego.

790 Dallard, T. & Spedding, G.R., 1993. 2-D wavelet transforms: generalisation of the Hardy
791 space and application to experimental studies, *Eur. J. Mech. B-Fluids*, **12**, 107-134.

792 Downey, N.J. & Gurnis, M., 2009. Instantaneous dynamics of the cratonic Congo basin, *J.*
793 *Geophys. Res.*, **114**, B06401, doi:10.1029/2008JB006066.

794 Farge, M., 1992. Wavelet transforms and their applications to turbulence, *Annu. Rev. Fluid*
795 *Mech.*, **24**, 395-457.

796 Gdeisat, M.A., Burton, D.R. & Lalor, M.J., 2006. Spatial carrier fringe pattern demodulation
797 by use of a two-dimensional continuous wavelet transform, *Appl. Optics*, **45**, 8722-8732.

798 Grossman, A. & Morlet, J., 1984. Decomposition of Hardy functions into square integrable
799 wavelets of constant shape, *SIAM J. Math. Anal.*, **15**, 723-736.

800 Hudgins, L., Friehe, C.A. & Mayer, M.E., 1993. Wavelet transforms and atmospheric
801 turbulence, *Phys. Rev. Lett.*, **71**, 3279-3282.

802 Kaiser, G., 1994. *A Friendly Guide to Wavelets*, Birkhäuser, Cambridge MA.

803 Kestin, T.S., Karoly, D.J., Yano, J.-I. & Rayner, N.A., 1998. Time–frequency variability of
804 ENSO and stochastic simulations, *J. Clim.*, **11**, 2258-2272.

805 Kirby, J.F., 2005. Which wavelet best reproduces the Fourier power spectrum? *Comput.*
806 *Geosci.*, **31**, 846-864.

807 Kirby, J.F. & Swain, C.J., 2004. Global and local isostatic coherence from the wavelet
808 transform, *Geophys. Res. Lett.*, **31**, L24608, doi:10.1029/2004GL021569.

809 Kirby, J.F. & Swain, C.J., 2006. Mapping the mechanical anisotropy of the lithosphere using
810 a 2D wavelet coherence, and its application to Australia, *Phys. Earth Planet. Inter.*, **158**,
811 122-138.

812 Kirby, J.F. & Swain, C.J., 2009. A reassessment of spectral T_e estimation in continental
813 interiors: the case of North America, *J. Geophys. Res.*, **114**, B08401,
814 doi:10.1029/2009JB006356.

815 Kirby, J.F. & Swain, C.J., 2011. Improving the spatial resolution of effective elastic thickness
816 estimation with the fan wavelet transform, *Comput. Geosci.*, **37**, 1345-1354.

817 Li, S., Su, X. & Chen, W., 2009. Spatial carrier fringe pattern phase demodulation by use of a
818 two-dimensional real wavelet, *Appl. Optics*, **48**, 6893-6906.

819 Pavlis, N.K., Holmes, S.A., Kenyon, S.C. & Factor, J.K., 2012. The development and
820 evaluation of the Earth Gravitational Model 2008 (EGM2008), *J. Geophys. Res.*, **117**,
821 B04406, doi:10.1029/2011JB008916.

822 Percival, D.P., 1995. On estimation of the wavelet variance, *Biometrika*, **82**, 619-631.

823 Perrier, V., Philipovitch, T. & Basdevant, C., 1995. Wavelet spectra compared to Fourier
824 spectra, *J. Math. Phys.*, **36**, 1506-1519.

825 Saupe, D., 1988. Algorithms for random fractals, in *The Science of Fractal Images*, pp. 71-
826 136, eds Peitgen, H.-O. & Saupe, D., Springer, New York.

827 Shyu, H.-C. & Sun, Y.-S., 2002. Construction of a Morlet wavelet power spectrum,
828 *Multidimens. Syst. Signal Process.*, **13**, 101-111.

829 Simons, F.J., Zuber, M.T. & Korenaga, J., 2000. Isostatic response of the Australian
830 lithosphere: Estimation of effective elastic thickness and anisotropy using multitaper
831 spectral analysis, *J. Geophys. Res.*, **105**(B8), 19,163-19,184.

832 Simons, F.J., van der Hilst, R.D. & Zuber, M.T., 2003. Spatiospectral localization of isostatic
833 coherence anisotropy in Australia and its relation to seismic anisotropy: Implications for
834 lithospheric deformation, *J. Geophys. Res.*, **108**(B5), 2250, doi:10.1029/2001JB000704.

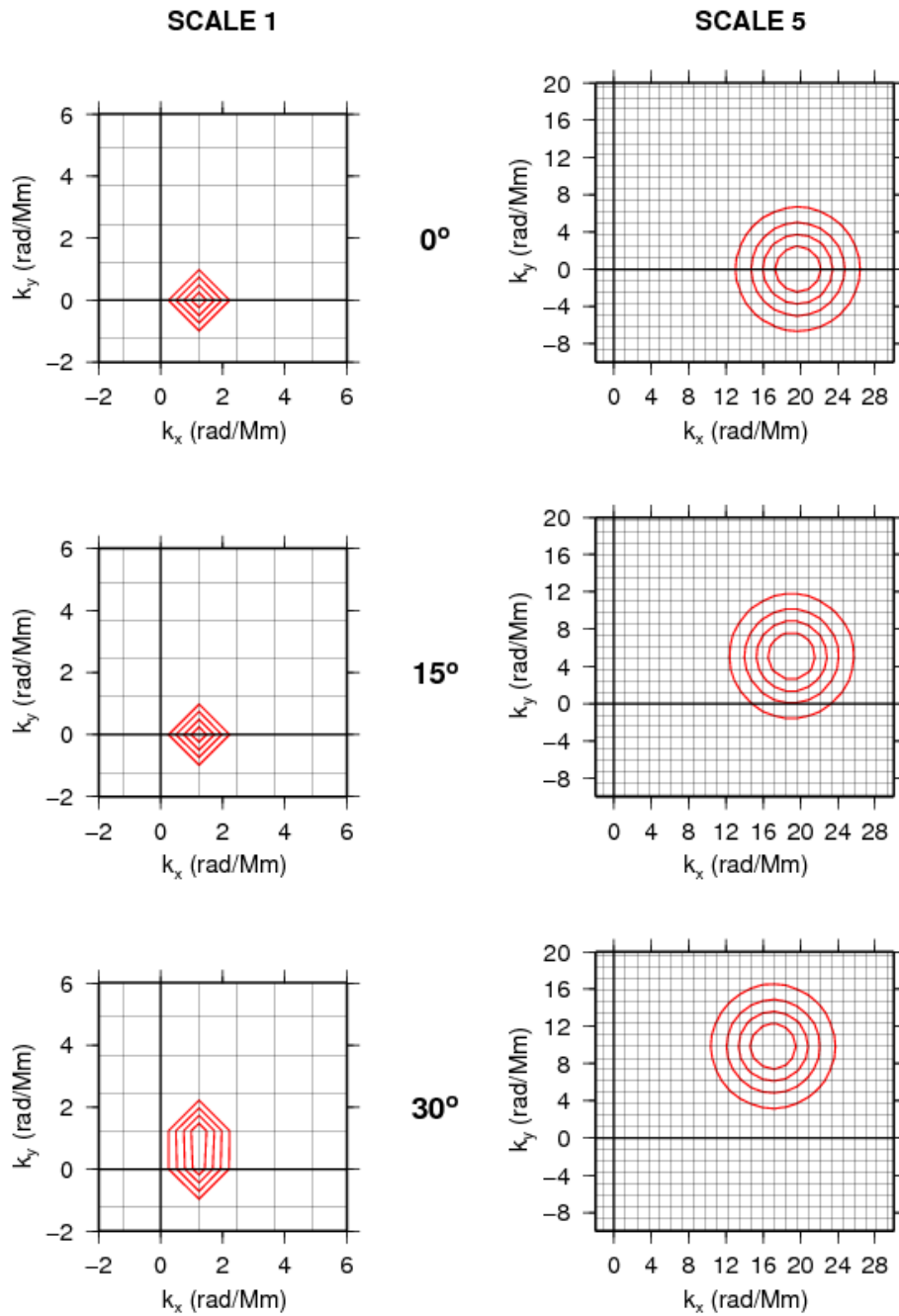
835 Simons, M., Solomon, S.C. & Hager, B.H., 1997. Localization of gravity and topography:
836 constraints on the tectonics and mantle dynamics of Venus, *Geophys. J. Int.*, **131**, 24-44.

837 Slepian, D., 1978. Prolate spheroidal wave functions, Fourier analysis, and uncertainty – V:
838 the discrete case, *Bell Syst. Tech. J.*, **57**, 1371-1430.

839 Thomson, D.J., 1982. Spectrum estimation and harmonic-analysis, *Proc. IEEE*, **70**, 1055-
840 1096.

841 Thomson, D.J., 2007. Jackknifing multitaper spectrum estimates, *IEEE Signal Process. Mag.*,
842 **24**, 20-30.

- 843 Thomson, D.J. & Chave, A.D., 1991. Jackknifed error estimates for spectra, coherences, and
844 transfer functions, in *Advances in Spectrum Analysis and Array Processing 1*, pp. 58-113,
845 ed. Haykin, S., Prentice Hall, Englewood Cliffs NJ.
- 846 Torrence, C. & Compo, G.P., 1998. A practical guide to wavelet analysis, *Bull. Amer.*
847 *Meteorol. Soc.*, **79**, 61-78.
- 848 Turcotte, D.L., 1997. *Fractals and Chaos in Geology and Geophysics*, 2nd edn, Cambridge
849 University Press, Cambridge.
- 850 Wiecek, M.A. & Simons, F.J., 2005. Localized spectral analysis on the sphere, *Geophys.*
851 *J. Int.*, **162**, 655-675.
- 852



853

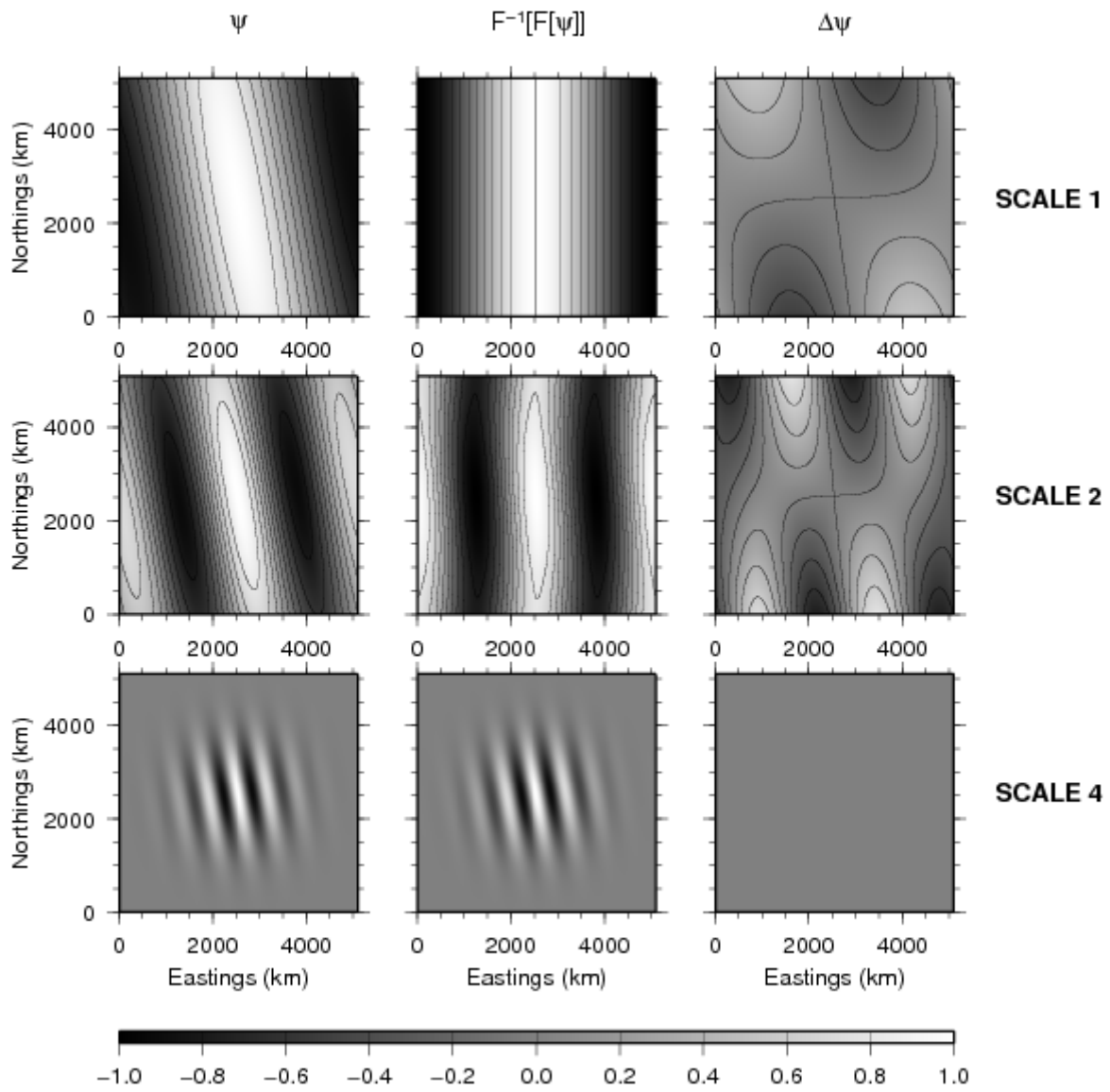
854 Figure 1. Three Morlet wavelets (red) of $|\mathbf{k}_0| = 5.336$ in the wavenumber domain, at azimuths

855 of 0° , 15° and 30° , and at two scales. Wavelet parameters are $N_x = N_y = 256$, $\Delta x = \Delta y = 20$

856 km, and 1 voice, giving a total of 7 scales, so scale 1 is the largest scale used in the analysis.

857 The grid mesh shows the discrete wavenumbers of this domain.

858



859

860 Figure 2. Space-domain 2D Morlet wavelets (real part) of $|\mathbf{k}_0| = 7.547$ and azimuth $\alpha = 10^\circ$,

861 at 3 scales, computed directly in the space domain (ψ) and by inverse Fourier transformation

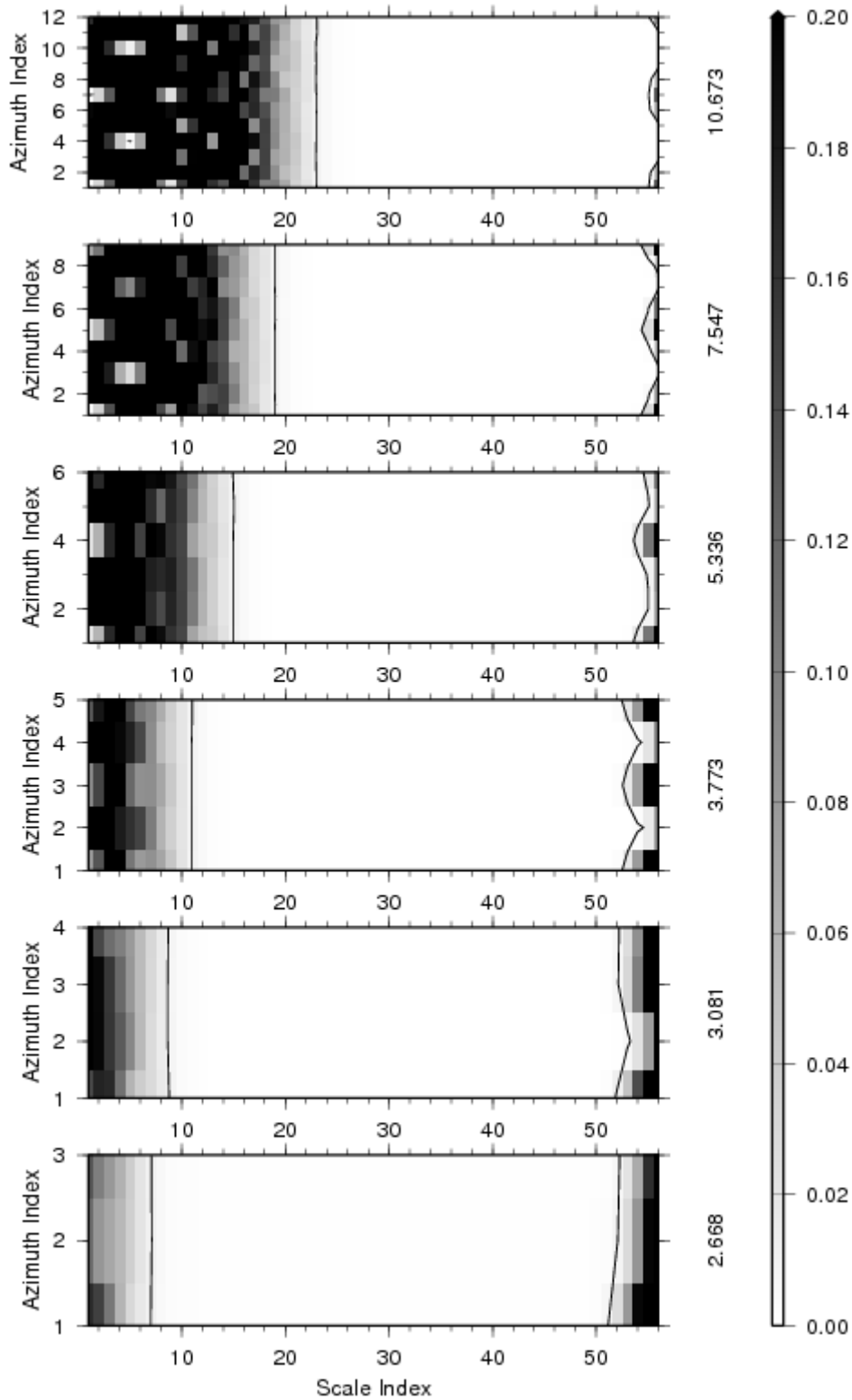
862 of the wavelet defined in the wavenumber domain ($\mathbf{F}_2^{-1}[\hat{\psi}]$), with the difference shown in the

863 third column. Wavelet parameters are $N_x = N_y = 256$, $\Delta x = \Delta y = 20$ km, and 1 voice, giving a

864 total of 7 scales. All wavelets are normalised to have a maximum amplitude of 1 unit.

865 Contouring is at 0.2 units.

866



867

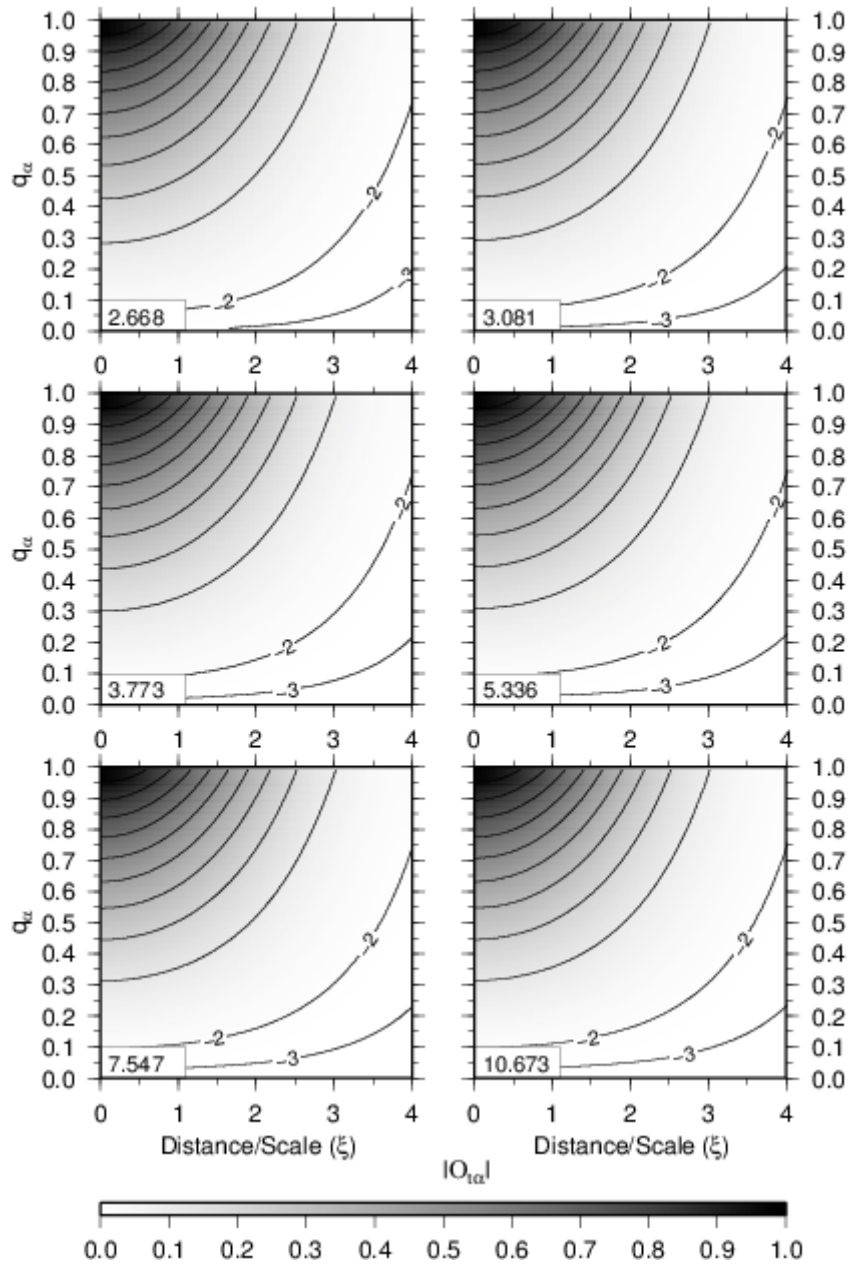
868 Figure 3. Plot of the energy difference between space-domain and inverse-transformed
 869 Fourier-domain wavelets, $\Delta E_{i,j}$, from eq. (23), versus scale index (j) and azimuth index (i), for
 870 the 2D Morlet wavelets (of indicated $|\mathbf{k}_0|$) comprising a Morlet-fan wavelet. Low values of
 871 scale index represent large-scale wavelets. The number of azimuths varies with $|\mathbf{k}_0|$, and

872 azimuth is computed using $\alpha_i = (i-1)\delta\alpha$, where $\delta\alpha$ is obtained from eq. (41) using $q_\alpha = e^{-1}$.

873 The $\Delta E_{ij} = 0.01$ contour is shown in black. Wavelet parameters are $N_x = N_y = 256$, $\Delta x = \Delta y =$

874 20 km, and 8 voices, giving a total of 56 scales.

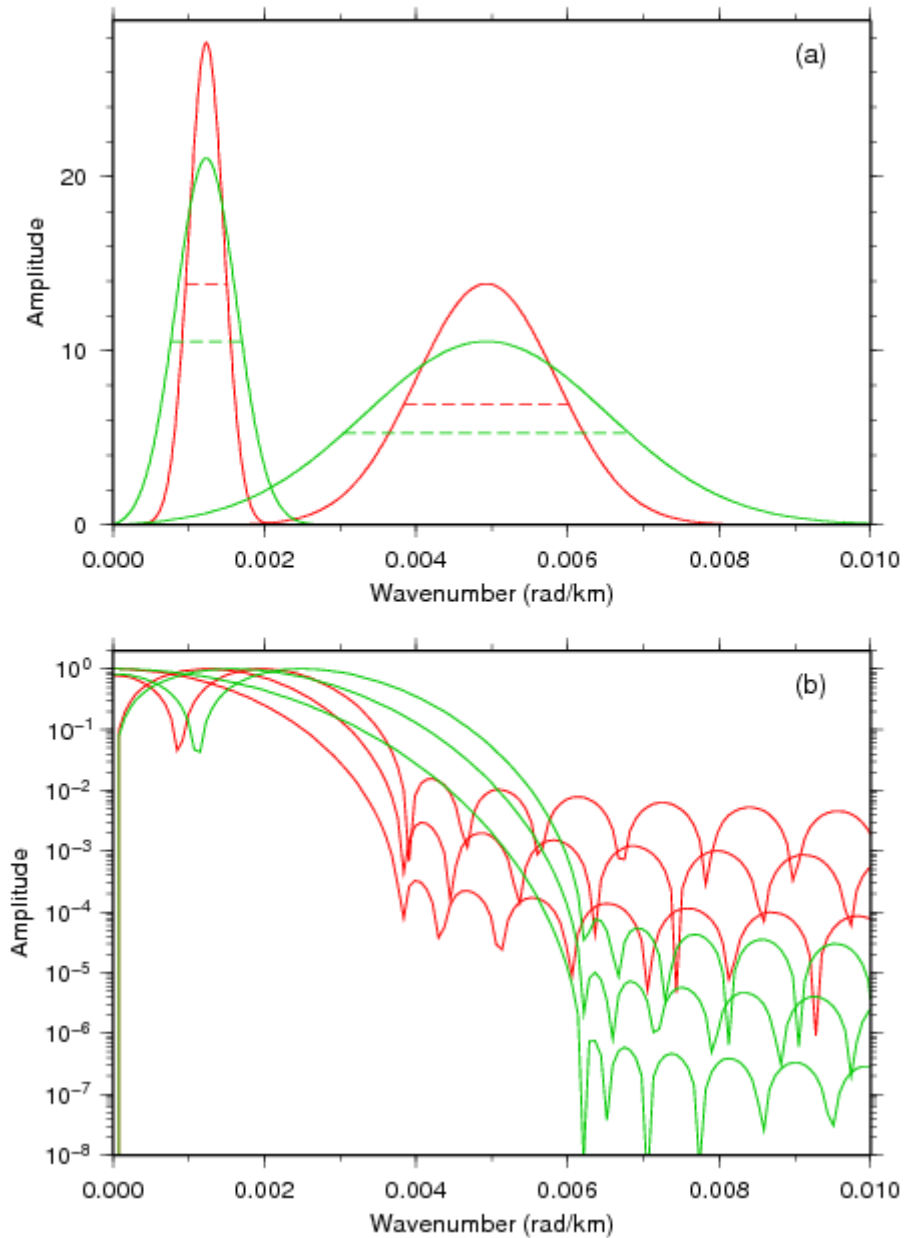
875



876

877 Figure 4. Plots of the degree of space-azimuth orthogonality modulus ($|O_{t\alpha}|$) from eq. (43) for
 878 two adjacent 2D Morlet wavelets of the same scale, for the indicated $|k_0|$ values. Wavelets at
 879 the same azimuth have $q_\alpha = 1$; spatially coincident wavelets have $\xi = 0$. Contour interval is
 880 0.1, except those annotated which show powers of 10.

881



882

883 Figure 5. Wavenumber-domain resolution of wavelets and Slepian tapers. Cross-sections

884 through amplitudes of 2D Morlet wavelets and Slepian tapers in the wavenumber domain. (a)

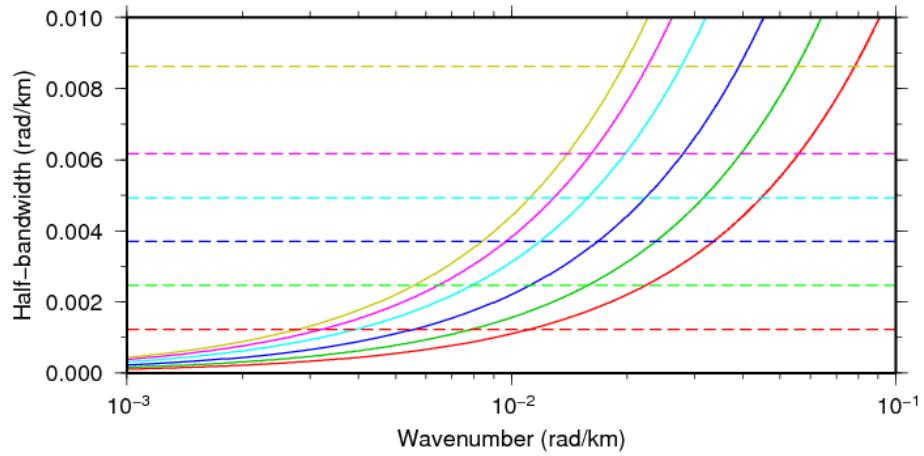
885 Morlet wavelets with $|\mathbf{k}_0| = 5.336$ (red) and 3.081 (green) at two scales; the full bandwidth is

886 shown by the dotted lines. (b) The first three Slepian tapers ($K = 1, 2, 3$) with $NW = 3$ (red)

887 and 5 (green); the $NW = 3$ bandwidth is $W = 3.7 \times 10^{-3} \text{ rad km}^{-1}$, the $NW = 5$ bandwidth is W

888 $= 6.1 \times 10^{-3} \text{ rad km}^{-1}$. Note the difference between the axes in the two images.

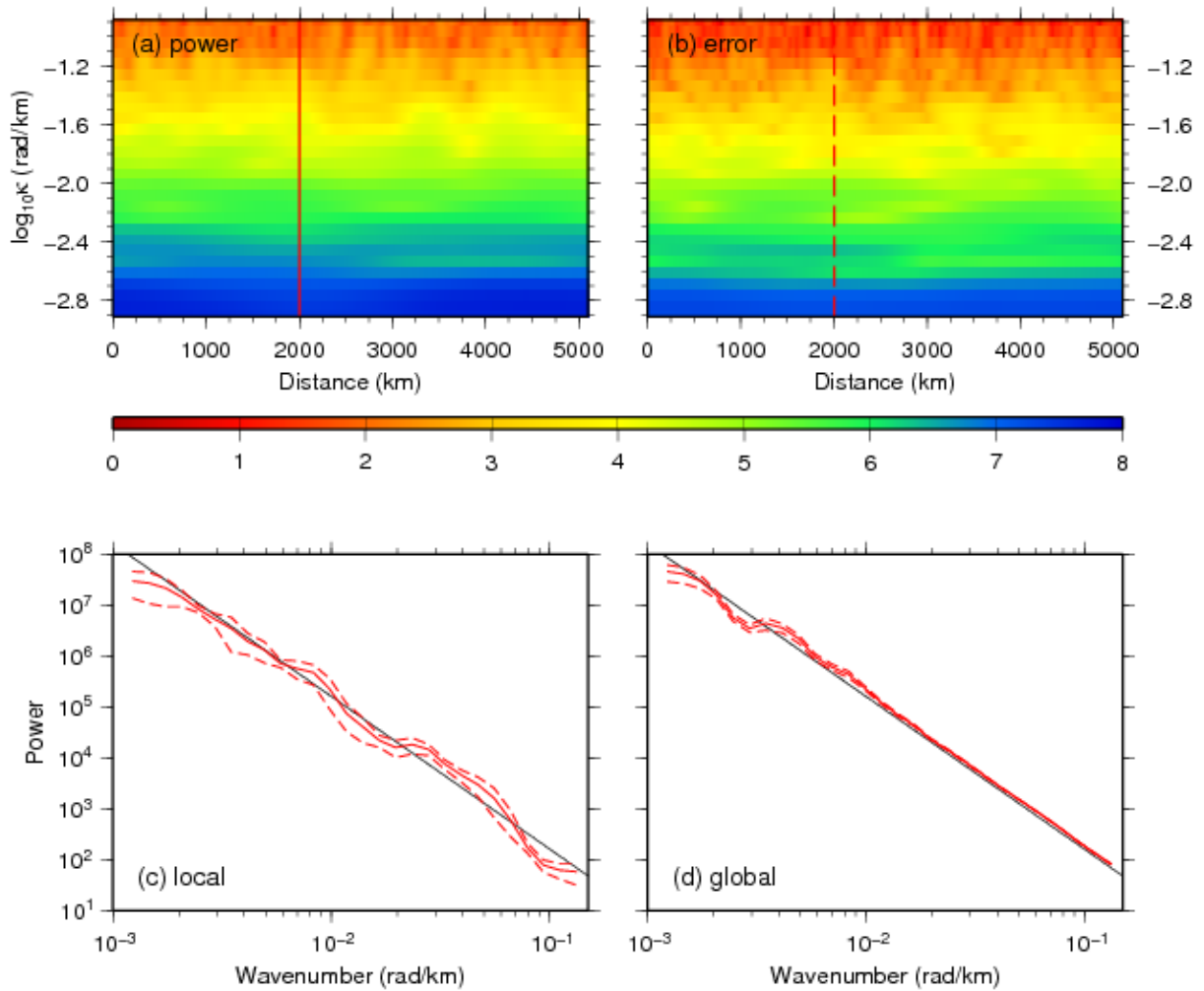
889



890

891 Figure 6. The half-bandwidth of Morlet wavelets (solid lines) and Slepian tapers (dashed
 892 lines). For Morlet wavelets: $|\mathbf{k}_0| = 10.673$ (red), 7.547 (green), 5.336 (blue), 3.773 (cyan),
 893 3.081 (magenta), 2.668 (gold) in eq. (62). For Slepian tapers: NW = 1 (red), 2 (green), 3
 894 (blue), 4 (cyan), 5 (magenta), 7 (gold), with $L = 5100$ km in eq. (63).

895



896

897 Figure 7. (a) A slice through the azimuthally-averaged fan wavelet scalogram for periodic

898 fractal model #001, using $|\mathbf{k}_0| = 5.336$. (b) The jackknifed error spectrum associated with (a).

899 Both slices are at 2540 km northing coordinate. Colour scale is \log_{10} power. (c) Local

900 wavelet power spectrum at the location of the vertical line in (a), i.e., at coordinate (2000 km

901 E, 2540 km N). The solid red line is the power from (a), the dashed red lines are the upper

902 and lower bounds on the power after addition/subtraction of the error in (b). (d) Global

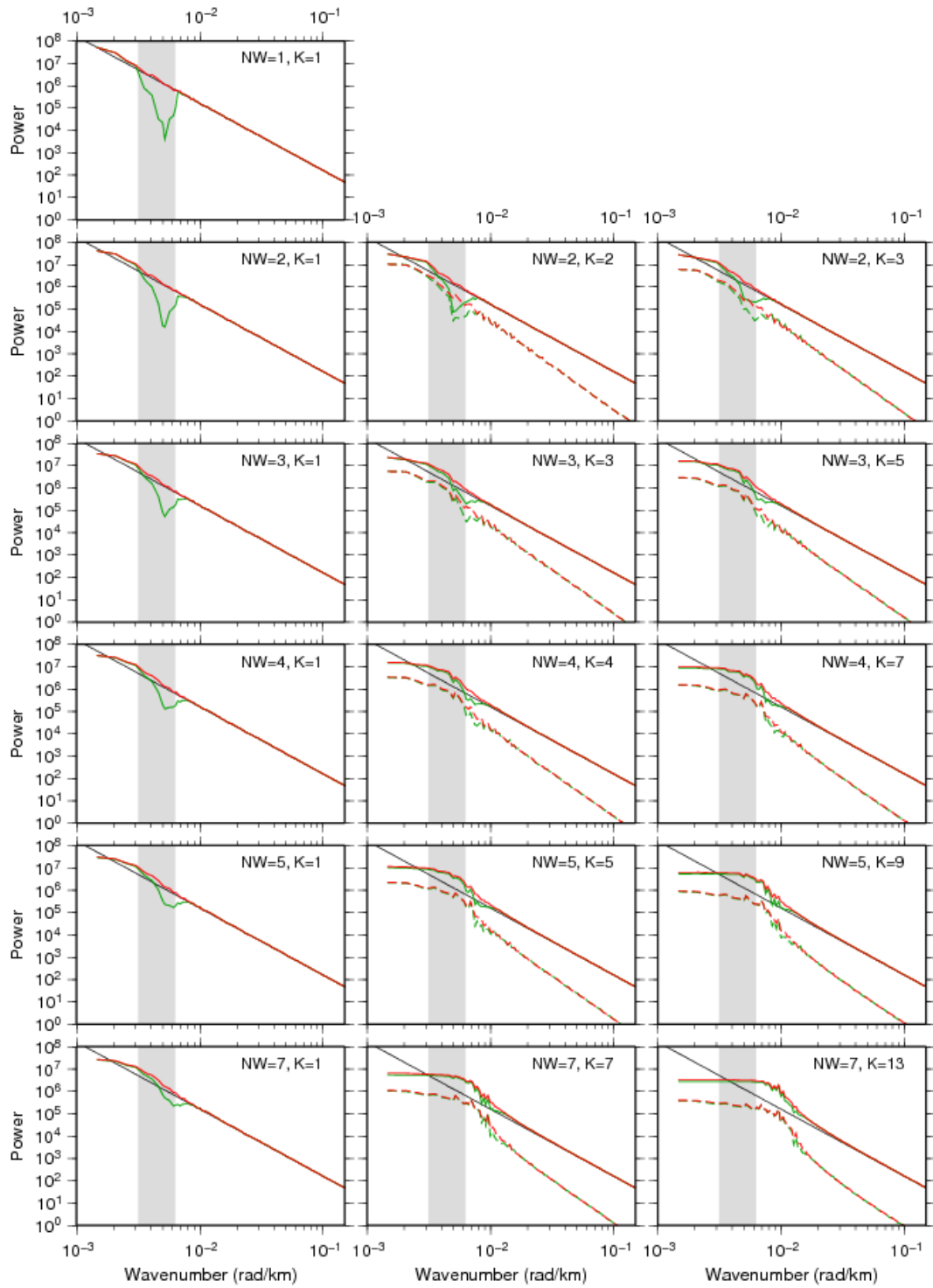
903 wavelet spectra for model #001. The solid red line is the global power spectrum, the dashed

904 red lines are the upper and lower bounds on the power after addition/subtraction of the global

905 error spectrum. In both (c) and (d) the black line is the theoretical fractal power spectrum,

906 illustrating the bias of the estimated spectra.

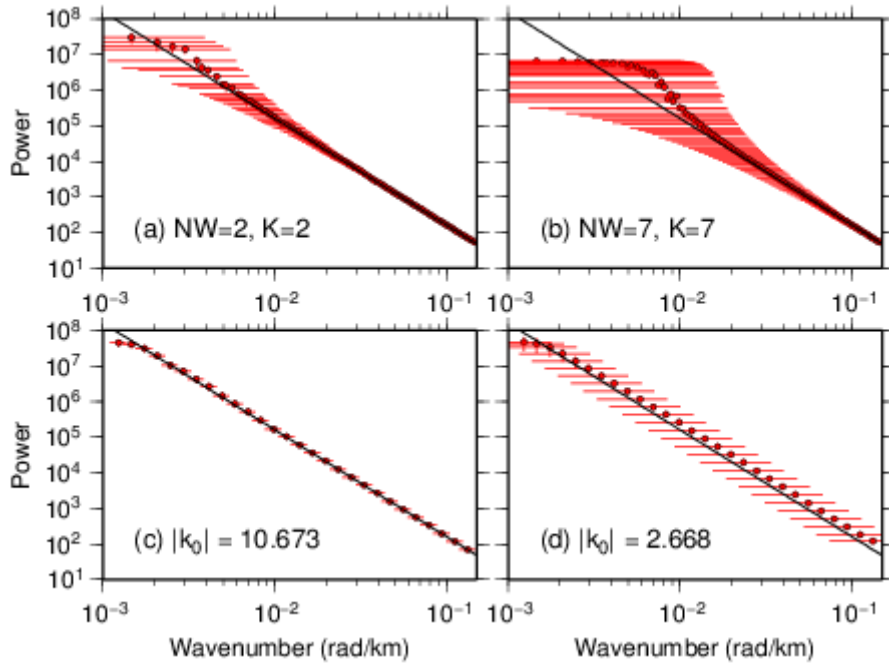
907



908

909 Figure 8. Multitaper power spectra for some selected NW and K values, of unfiltered (red)
 910 and filtered (green) periodic fractal surfaces. The filtered data have been frequency-filtered
 911 using a cosine function which suppresses harmonics between 1000 and 2000 km wavelength
 912 (the 'block-band', grey shading). Power spectra are solid lines; errors are dashed. The spectra
 913 and errors are the arithmetic means of the individual spectra from 100 random fractal models.

914 The theoretical fractal power spectrum is shown in black. No jackknife errors are available
915 when there is only one taper.
916



917

918 Figure 9. (a) and (b) Two of the spectra in Fig. 8 from the MT method showing error bars in

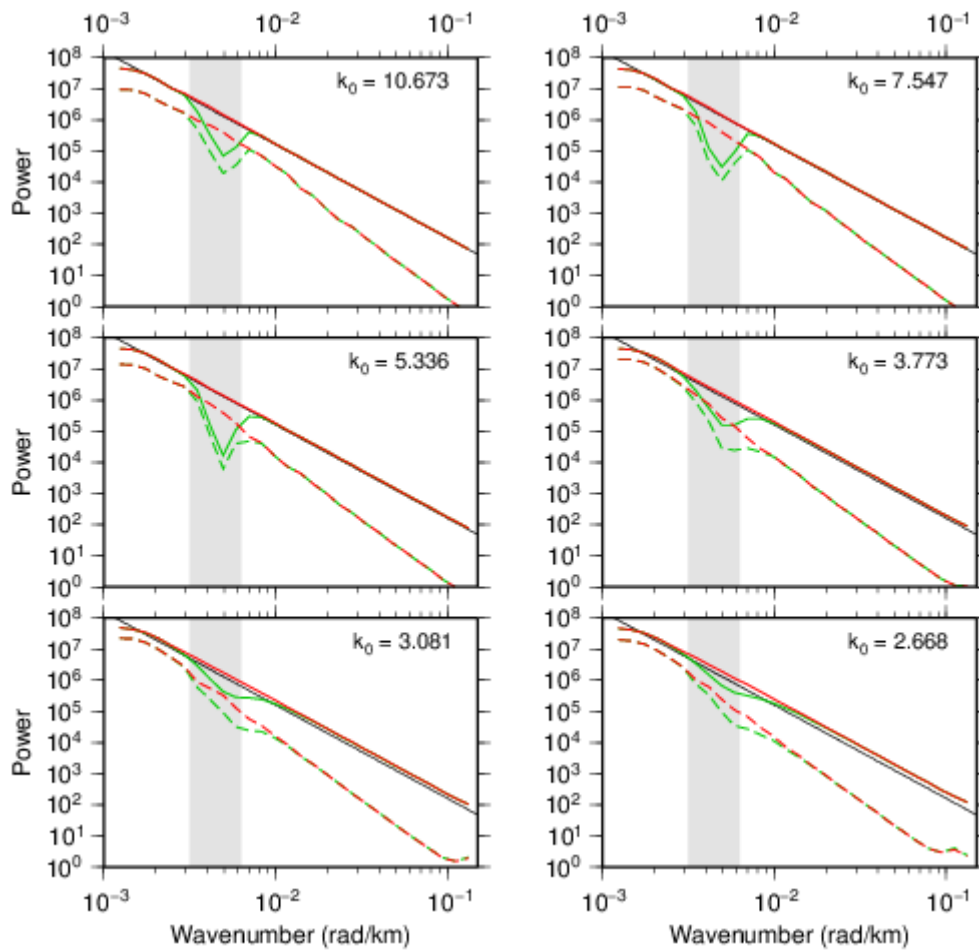
919 power and wavenumber. The wavenumber error bars are computed from (63). (c) and (d)

920 Two of the spectra in Fig. 10 from the fan-WT method showing error bars in power (too

921 small to register on this scale) and wavenumber. The wavenumber error bars are computed

922 from eq. (62).

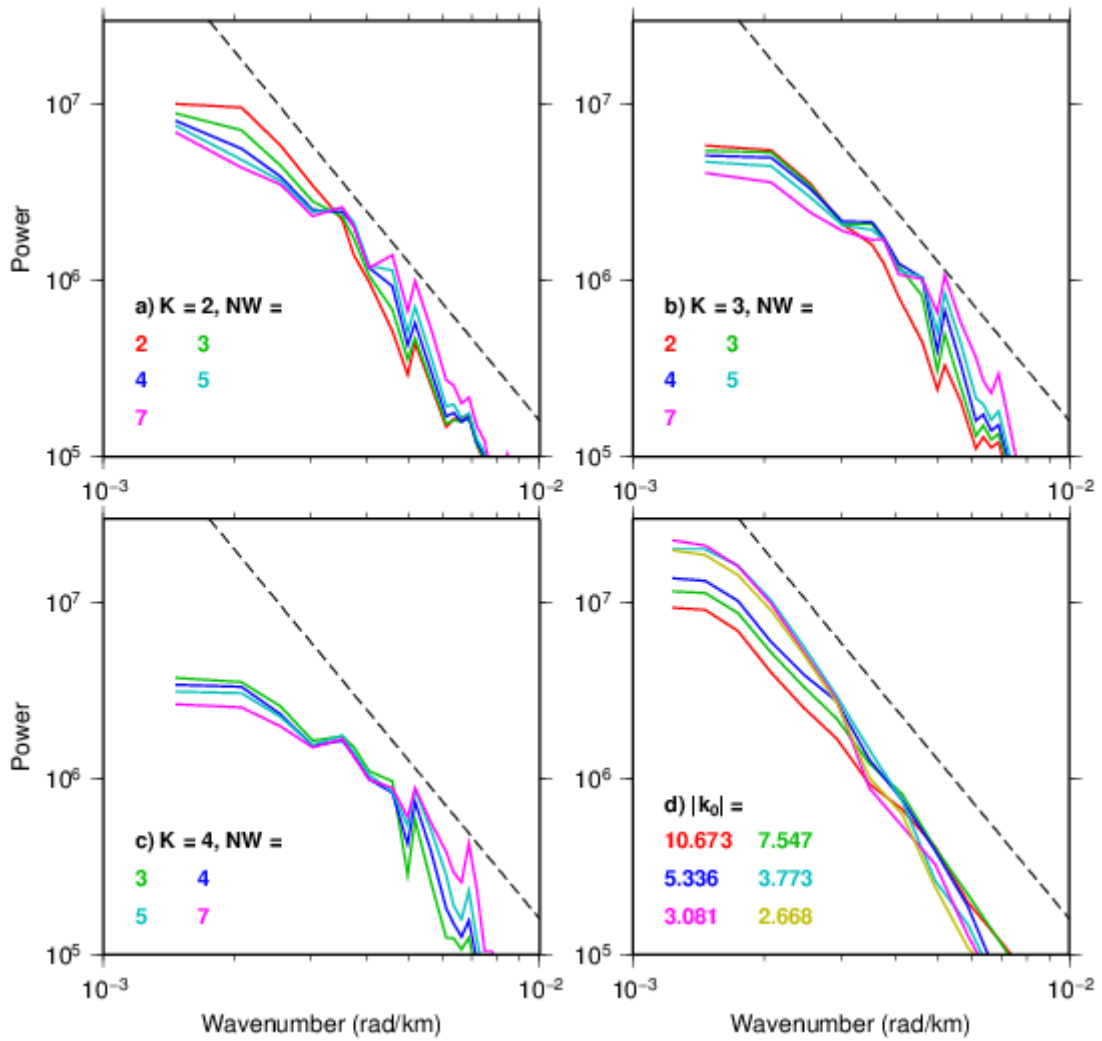
923



924

925 Figure 10. Global wavelet power spectra for some $|k_0|$ values, of unfiltered (red) and filtered
 926 (green) periodic fractal surfaces (see Fig. 8 caption). Power spectra are solid lines; errors are
 927 dashed. The spectra and errors are the arithmetic means of the individual spectra from 100
 928 random fractal models. The theoretical fractal power spectrum is shown in black.

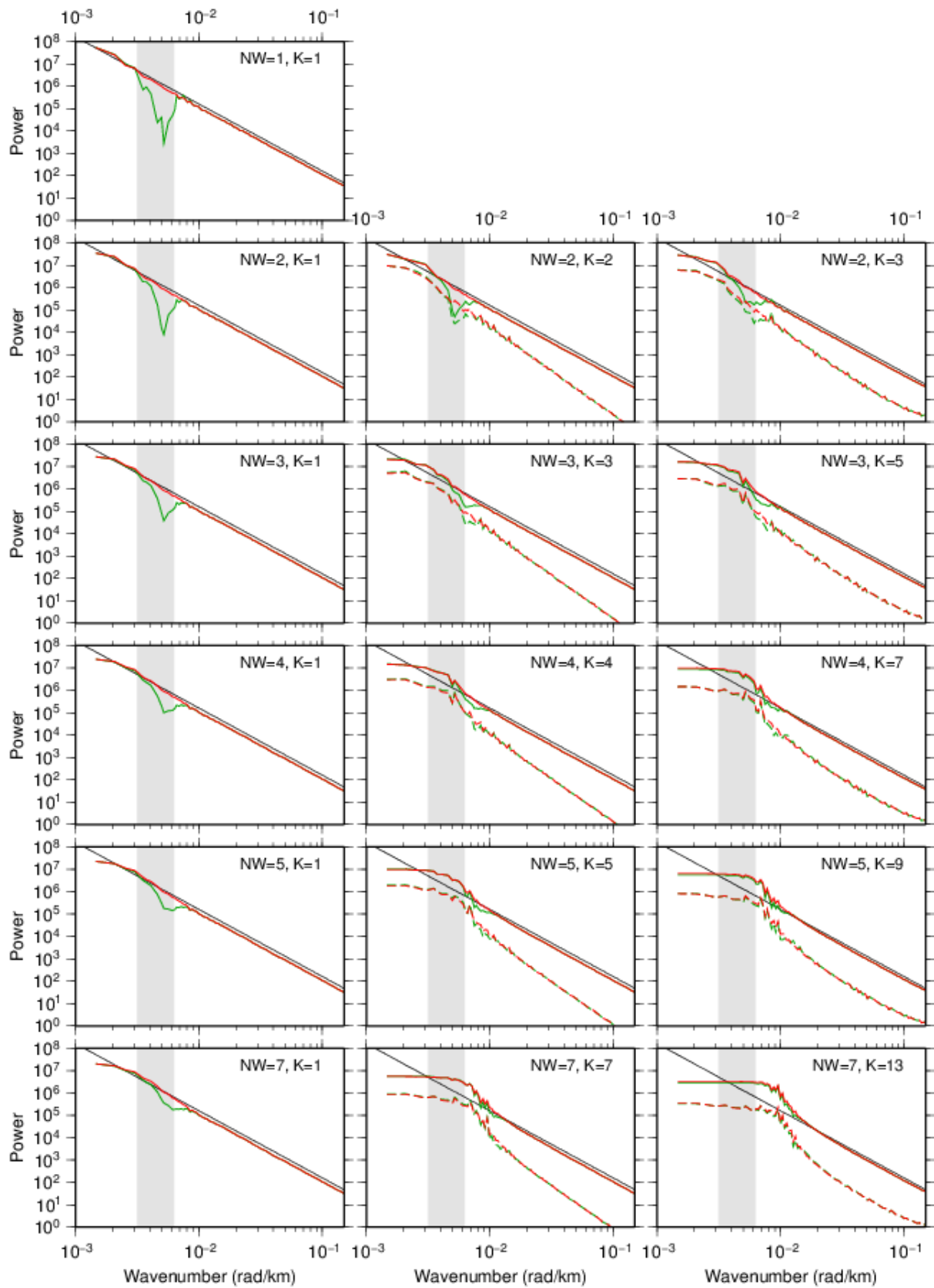
929



930

931 Figure 11. Power spectrum errors from the (a) – (c) multitaper method at the indicated NW
 932 and K values, and (d) from the wavelet method at the indicated $|k_0|$ values. The dashed black
 933 line is the theoretical fractal power spectrum.

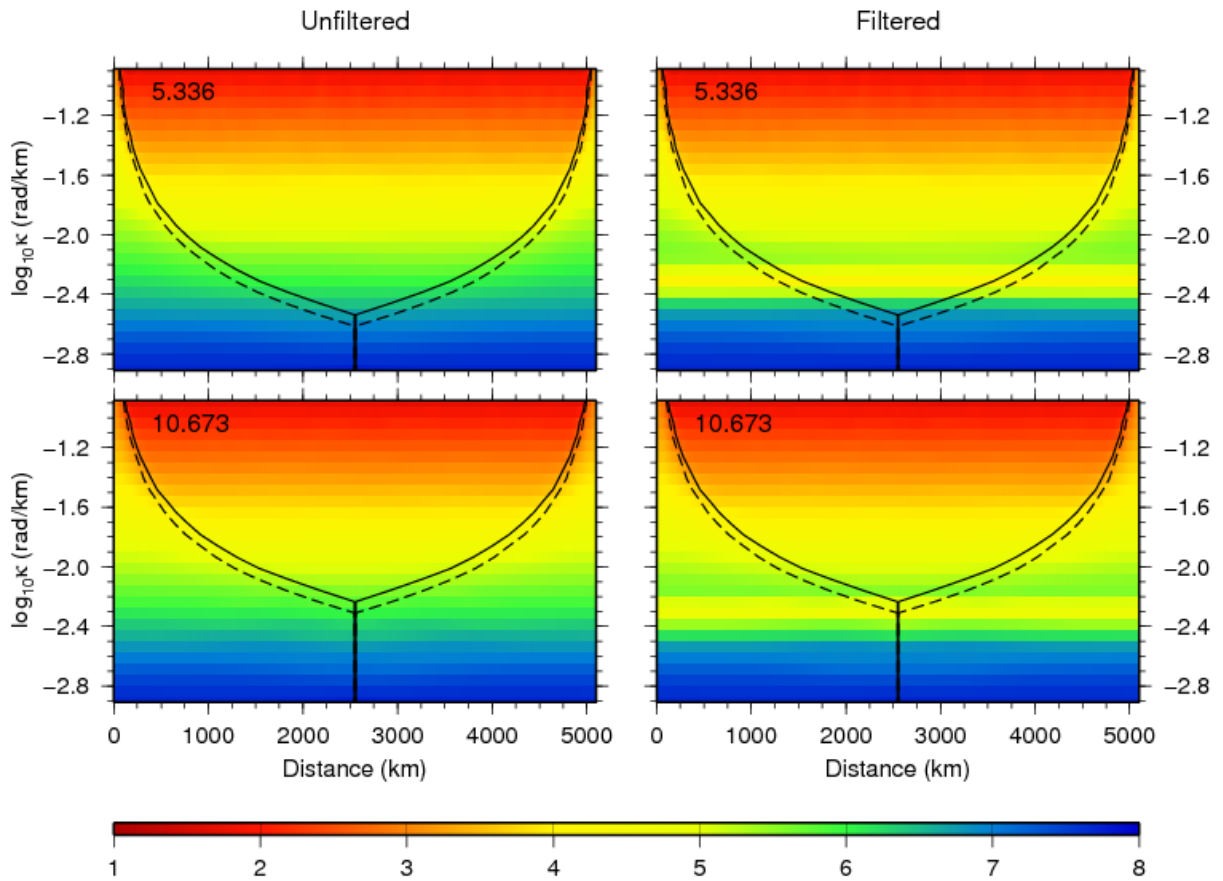
934



935

936 Figure 12. As Fig. 8, but for non-periodic data.

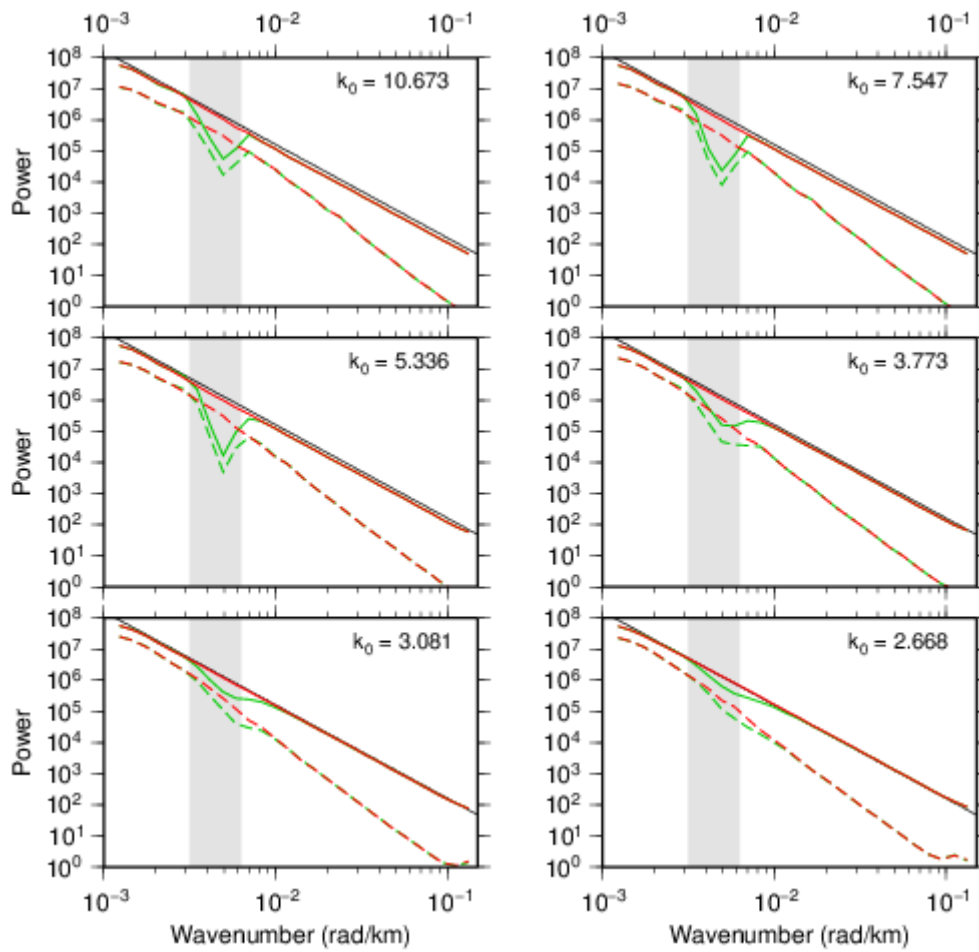
937



938

939 Figure 13. Slices through azimuthally-averaged local fan wavelet scalograms, averaged over
 940 100 models, of non-periodic unfiltered (left) and filtered (right) data, for the two indicated
 941 $|k_0|$ values. The slices are at 2540 km northing coordinate. The solid black lines show the
 942 cone of influence using the e^{-1} definition of Section 2.4, the dashed black lines show that
 943 from the half-amplitude definition. Colour scale is \log_{10} power.

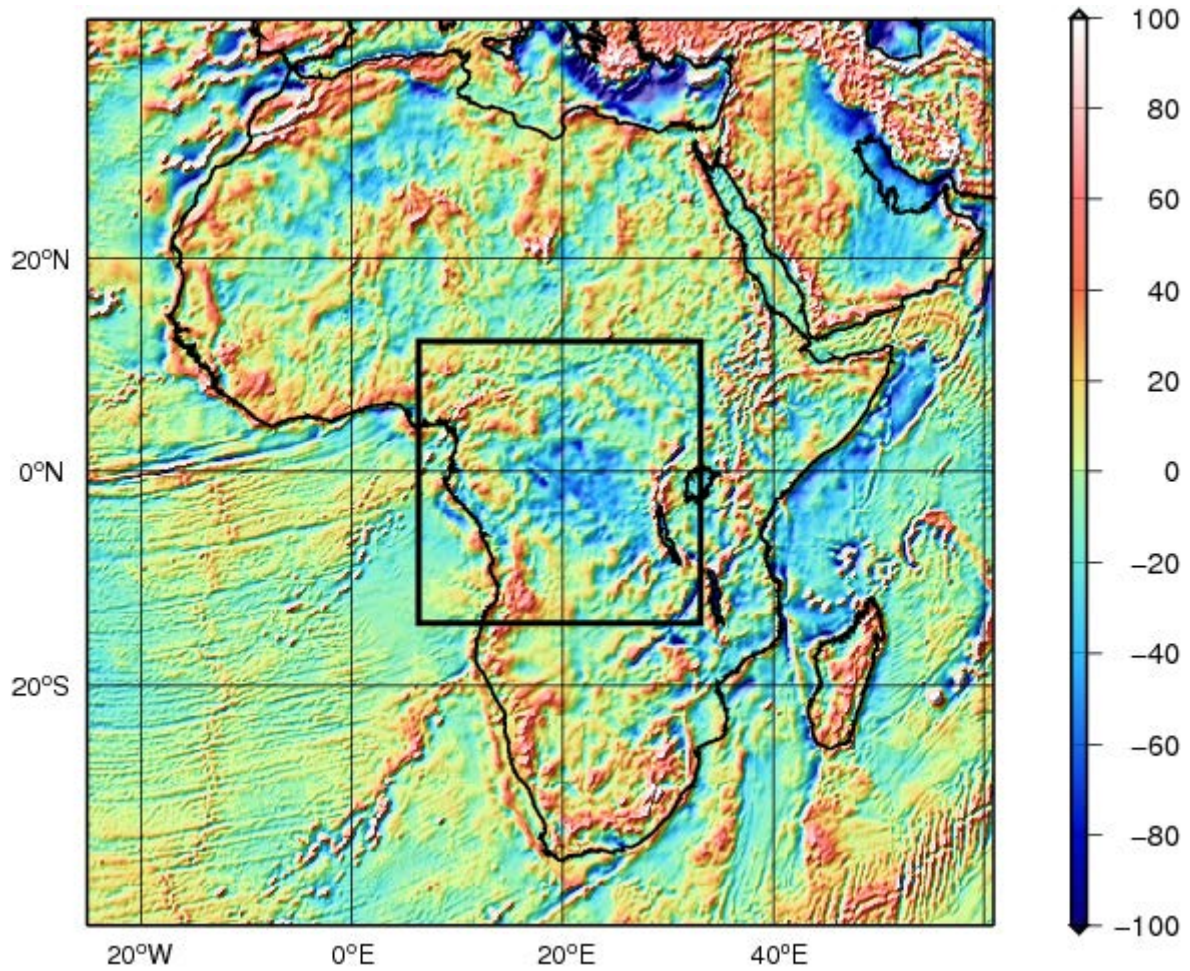
944



945

946 Figure 14. As Fig. 10, but for non-periodic data. An e^{-1} cone of influence was applied to the
 947 local scalograms before computation of the global wavelet power spectra.

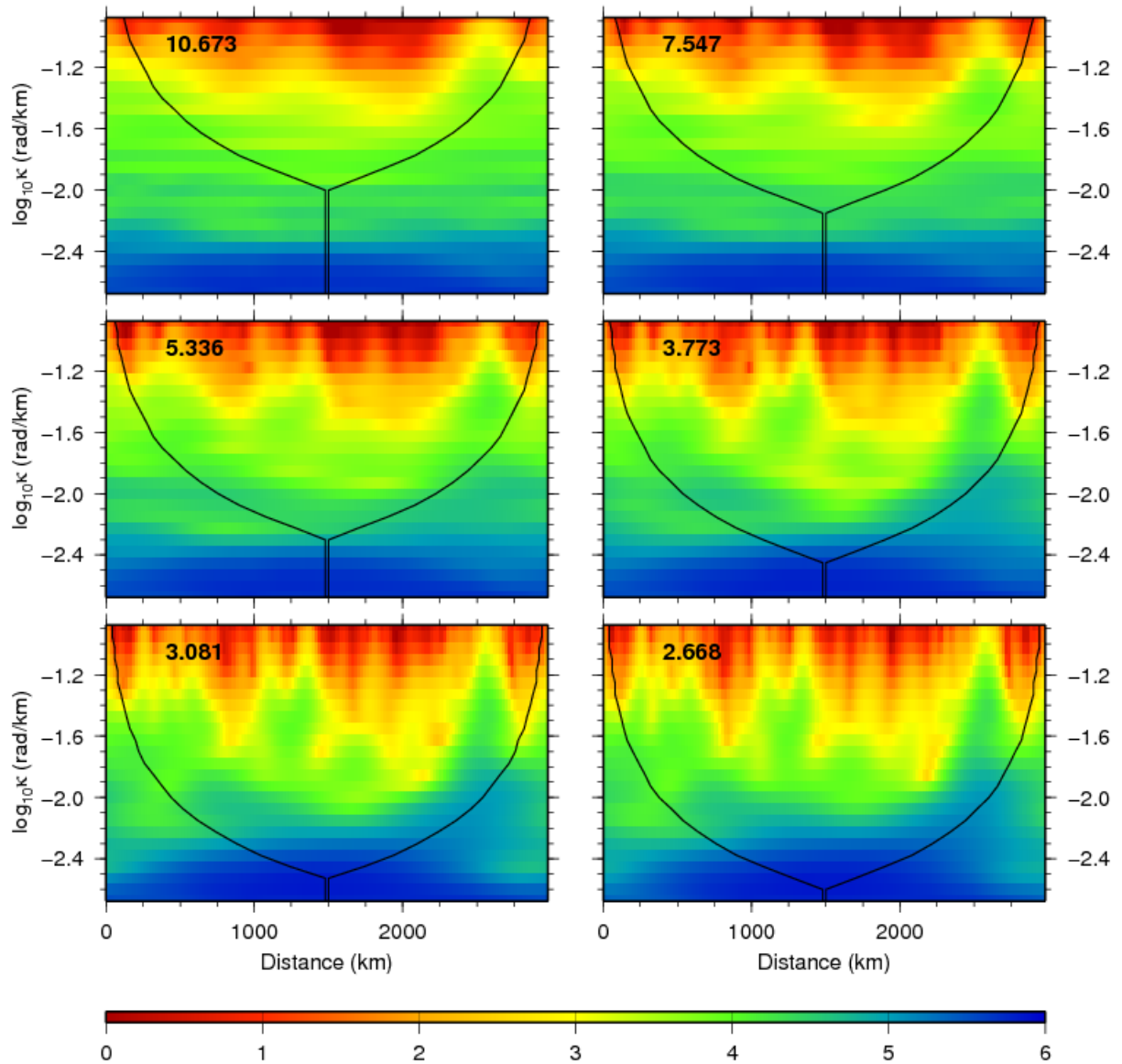
948



949

950 Figure 15. Free air gravity anomaly image for Africa and surrounding oceans derived from
 951 EGM2008 spherical harmonic coefficients (Mercator projection). The black box shows the
 952 smaller area of central Africa used for the spectra in Figs 16-19. Units are mGal.

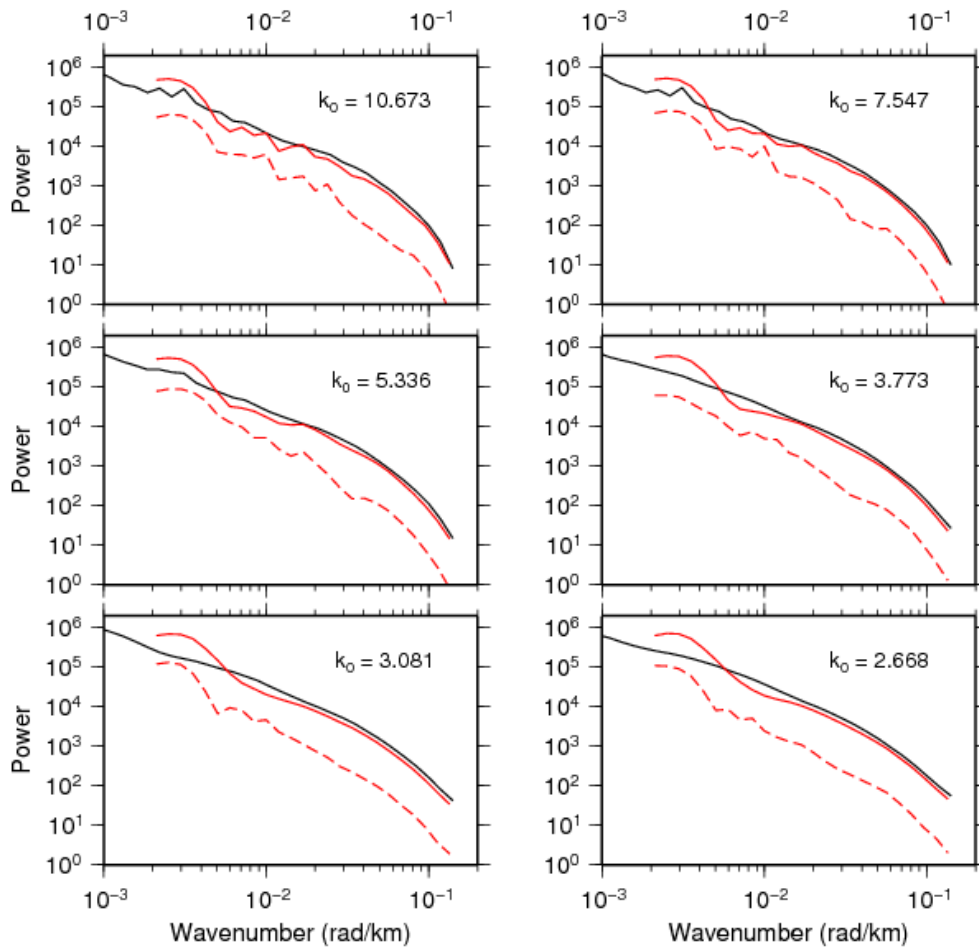
953



954

955 Figure 16. Slices through azimuthally-averaged local fan wavelet scalograms of the Congo
 956 basin free air anomaly, for the indicated $|\mathbf{k}_0|$ values. The slices run from west to east across
 957 the $\sim 1^\circ\text{S}$ parallel in the box in Fig. 15. The black lines show the cone of influence using the
 958 e^{-1} definition; only data within the cones are used to form the global wavelet spectra. Colour
 959 scale is \log_{10} power.

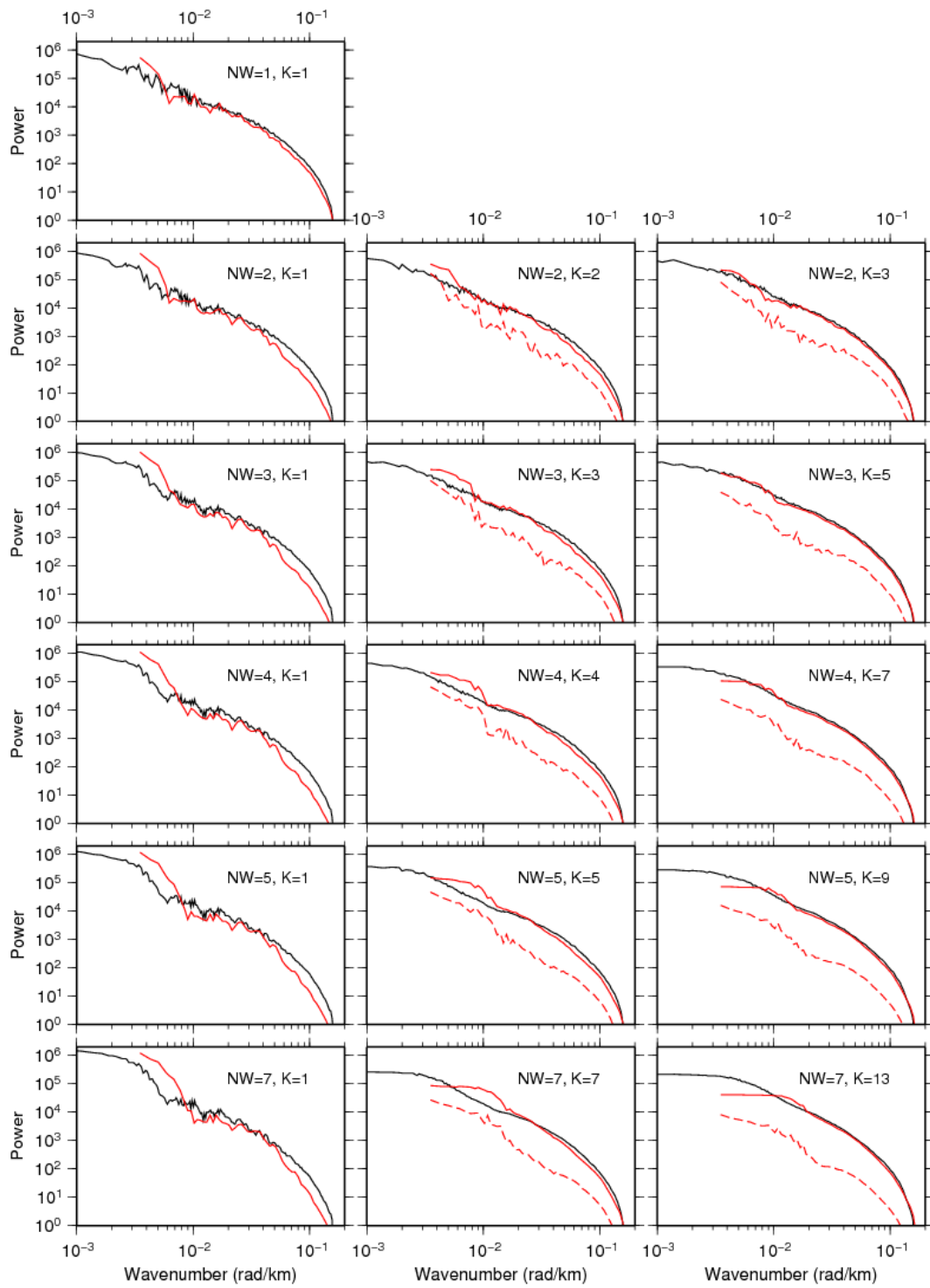
960



961

962 Figure 17. Global wavelet power spectra (solid lines), using six different $|\mathbf{k}_0|$ values, of the
 963 free air anomaly data in Fig. 15; errors are dashed lines. The red lines are for the 3000 km
 964 square box in Fig. 15 and the longer black lines are the spectra for the whole data set (~9000
 965 km square). The wavelet calculations use convolution (see Section 5) and an e^{-1} cone of
 966 influence (see Section 9.4).

967

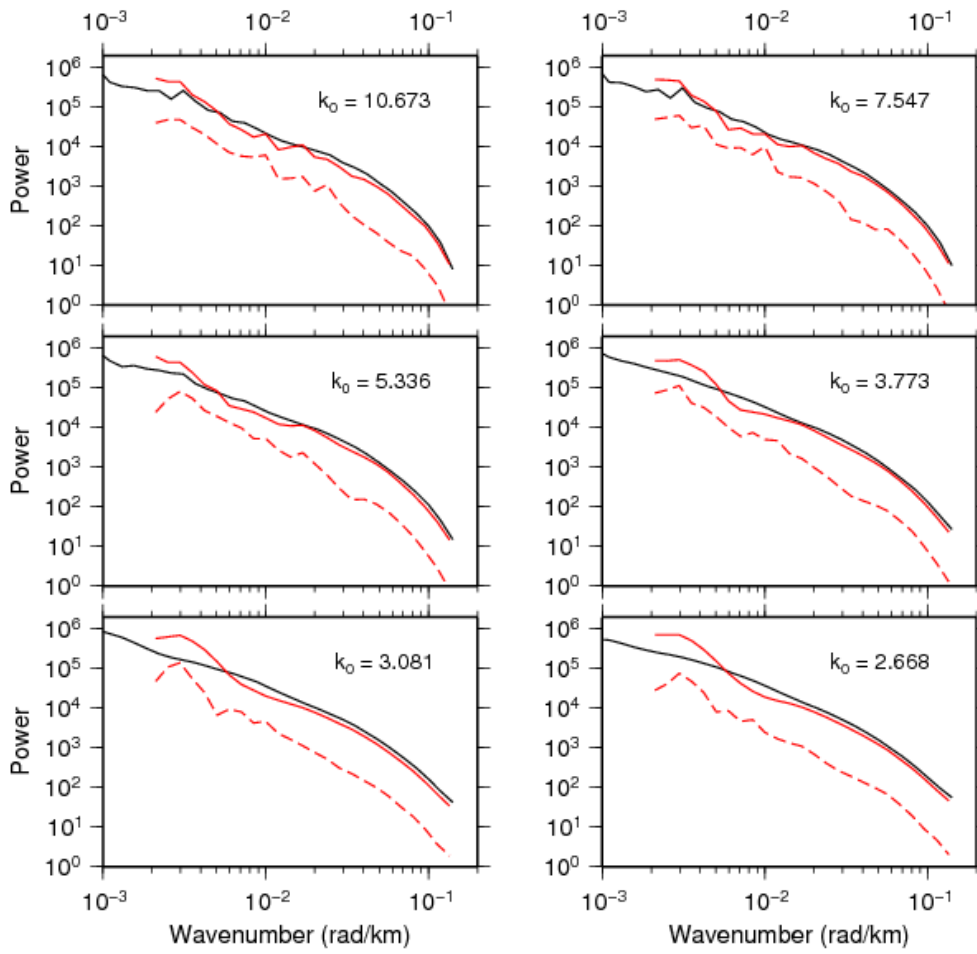


968

969 Figure 18. Multitaper power spectra, for some NW and K values, of the free air gravity data

970 shown in Fig. 15 (see caption for Fig. 17 for other details).

971



972

973 Figure 19. As Fig. 17, but for global wavelet power spectra computed using the Fourier
 974 method instead of using convolution.

975